A window into an older orogenic cycle: P-T conditions and timing of the pre-Alpine history of the Dora-Maira Massif (Western Alps)

Francesco Nosenzo, Paola Manzotti, Marc Poujol, Michel Ballèvre, Jessica Langlade

Received: 1 June 2021 | Revised: 28 October 2021 | Accepted: 5 November 2021

DOI: 10.1111/jmg.12646

ORIGINAL ARTICLE

Journal of METAMORPHIC GEOLOGY WILEY

A window into an older orogenic cycle: *P–T* conditions and timing of the pre-Alpine history of the Dora-Maira Massif (Western Alps)

Francesco Nosenzo[1] | **Paola Manzotti**[1] | **Marc Poujol**[2] | **Michel Ballèvre**[2] | **Jessica Langlade**[3]

[1]Department of Geological Sciences, Stockholm University, Stockholm, Sweden

[2]University of Rennes 1, CNRS, Géosciences Rennes-UMR 6118, F-35000, Rennes, France

[3]Microsonde Ouest, Ifremer-Centre de Bretagne, Technopole Brest Iroise, Plouzané, France

Correspondence
Francesco Nosenzo, Department of Geological Sciences, Stockholm University, 106 91 Stockholm, Sweden.
Email: francesco.nosenzo@geo.su.se

Funding information
Jubileumsdonationen K & A Wallenbergs Stiftelse; Swiss National Science Foundation; Stockholm University

Handling Editor: Prof. Clare Warren

Abstract

Deciphering the pre-orogenic evolution of subducted continental basement is challenging due to pervasive reworking of crust during subduction and exhumation. Survival of such polycyclic basement may occur locally in low strain domains bounded by intensely overprinted rocks. The Palaeozoic history of basement involved in Alpine continental subduction is investigated in the northern Dora-Maira Massif where a kilometre-scale domain of low strain preserves a pre-Alpine amphibolite-facies foliation in garnet-biotite orthogneiss and garnet-staurolite micaschist. By contrast, a first generation garnet is the only pre-Alpine relict in pervasively reworked domains surrounding the low-strain domain. Thermodynamic modelling based on garnet isopleths in micaschist constrains the pre-Alpine pressure–temperature (*P–T*) evolution from 4 to 5 kbar and ~500°C to 6–7 kbar and ~650°C, which is consistent with Barrovian metamorphism up to the staurolite zone. In this micaschist, monazite included in garnet rims provide an age of 324 ± 6 Ma (95% confidence interval; c.i.). On the basis of textural and chemical data, this is interpreted as recording peak Barrovian metamorphic conditions. Low Th/U metamorphic zircon overgrowths and crystals yield an age of 304 ± 2 Ma (95% confidence interval). On the basis of the trace element concentrations and rare earth element (REE) patterns measured in garnet and metamorphic zircon, the latter is tentatively interpreted as having grown during early exhumation or cooling, involving garnet consumption and fluid infiltration. The reconstructed Variscan Barrovian metamorphism of the northern Dora-Maira basement is consistent with that documented in the External Crystalline Massifs and in the Austroalpine domain of the Alps. The Palaeozoic basement of the Dora-Maira Massif likely represents upper crustal material, later involved in Alpine continental subduction under high- to ultra-high-pressure conditions.

KEYWORDS
Alps, Barrovian metamorphism, Dora-Maira, pre-Alpine history, thermodynamic modelling

1 | INTRODUCTION

During continental subduction, the pre-orogenic basement is in most cases pervasively reworked. Intense ductile deformation close to or at eclogite-facies conditions, as well as at lower pressure–temperature (*P–T*) conditions during exhumation, leads to the obliteration of pre-orogenic structures, and complete recrystallization of the basement. It is therefore a challenge to investigate the pre-orogenic history of the basement, for which our tools are relatively limited.

The lower continental crust is generally characterized by rocks that experienced high temperature metamorphism associated with partial melting. When subsequently subjected to a new orogenic cycle, dry, pre-orogenic, granulite-facies rocks are partially converted into eclogite-facies assemblages, mainly due to fluid infiltration along localized shear zones. Worldwide-known examples of granulite- to eclogite-facies transitions have been described in the Norwegian Caledonides (e.g. Austrheim, 1987, 2013; Bowhany et al., 2018; Erambert & Austrheim, 1993; Jamtveit et al., 1991) and the Musgrave Ranges, central Australia (Camacho et al., 1997; Ellis & Maboko, 1992). In such dry environments, eclogite-facies deformation may be accompanied by the development of pseudotachylite (e.g. Hawemann et al., 2018; Lund & Austrheim, 2003).

In high-pressure to ultra-high-pressure (*HP-UHP*) domains involving middle to upper crustal protoliths, most lithologies are converted into *HP-UHP* assemblages, making it difficult to find significant relicts of the pre-orogenic history. One may look for potential relicts of pre-orogenic minerals, especially multistage garnet (e.g. Brandt & Schenk, 2020; Feenstra et al., 2007; Le Bayon et al., 2006; Manzotti & Ballèvre, 2013) and zircon (e.g. Corfu et al., 2003; Kunz et al., 2018) that may have escaped complete dissolution and/or diffusional re-equilibration during the new orogenic cycle. Another approach is to identify, after careful and detailed mapping, low-strain domains where significant volumes (from a few m^3 to a few hundreds of m^3) of basement rocks have escaped pervasive recrystallisation during the ensuing orogenic cycle (e.g. Gosso et al., 2015; Krabbendam et al., 2000; Ramsay & Allison, 1979).

Three main types of low-strain domains may be distinguished (Figure 1). In the first type, small volumes of coarse-grained granitic or gabbroic rocks retain their magmatic texture and are only partially re-equilibrated at eclogite-facies conditions. Examples of this process have been described in the Western Alps, for example in the Sesia Zone (Monte Mucrone granite: Cenki-Tok et al., 2011; Compagnoni & Maffeo, 1973; Früh-Green, 1994; Koons et al., 1987) and the Dora-Maira Massif (Brossasco granite: Biino & Compagoni, 1992; Lenze & Stöckhert, 2007) and in the Dabie Shan, China (Zhang & Liou, 1997).

A second type of low-strain domain contains upper crustal rocks that have been dehydrated due to contact metamorphism associated with high level granitic intrusions or due to partial melting during high-temperature/low pressure regional metamorphism. Partially eclogitised rocks belonging to this category include high-grade gneisses and hornfelses from the Western Alps (Dora-Maira: Compagnoni et al., 1995; Compagnoni & Rolfo, 2003; Gran Paradiso: Gabudianu Radulescu et al., 2011; Monte Rosa: Bearth, 1952; Dal Piaz, 2001; Vaughan-Hammon et al., 2021) and low pressure cordierite-bearing migmatites of Ordovician age preserved in the core of the Carboniferous Variscan belt (e.g. Godard, 2009).

In this paper, we describe a third type of low-strain domain. Distinct from the previous examples, which were wholly made of coarse-grained plutonic rocks or dry high-grade metamorphic rocks, the third type of low-strain domain consists of pre-orogenic orthogneisses and micaschists retaining most of their older character. Few examples of this type have been fully characterized, and we illustrate them with a field example from the northern Dora-Maira Massif. There, well-preserved pre-Alpine mineralogical and structural relicts (Borghi et al., 1985; Vialon, 1966) were assumed to be developed at amphibolite (5–6 kbar, 600–650°C: Cadoppi, 1990) or granulite facies (4–7 kbar, 650–700°C: Bouffette et al., 1993). We provide here *for the first time* a quantitative reconstruction of the P–T history and isotopic age of the pre-orogenic basement in this fragment of subducted continental crust.

2 | GEOLOGICAL SETTING

2.1 | Geology of the Dora-Maira Massif

The Dora-Maira Massif in the Western Alps (Figure 2) belongs to the Briançonnais microcontinent, and it is now stacked below the remnants of the Piemonte-Liguria Ocean (Handy et al., 2010; Lardeaux et al., 2006; Schmid et al., 2004). It consists of a Palaeozoic basement and minor Mesozoic cover rocks (Ballèvre et al., 2020; Gasco et al., 2011; Michard, 1967; Sandrone et al., 1993; Vialon, 1966). The internal structure of the Dora-Maira Massif comprises a stack of coherent tectonic units distinguished on a lithological and petrological basis (Figure 2). The Pinerolo Unit is the structurally lowest element and is made of Upper Carboniferous graphite-rich meta-sediments intruded by Permian granites and

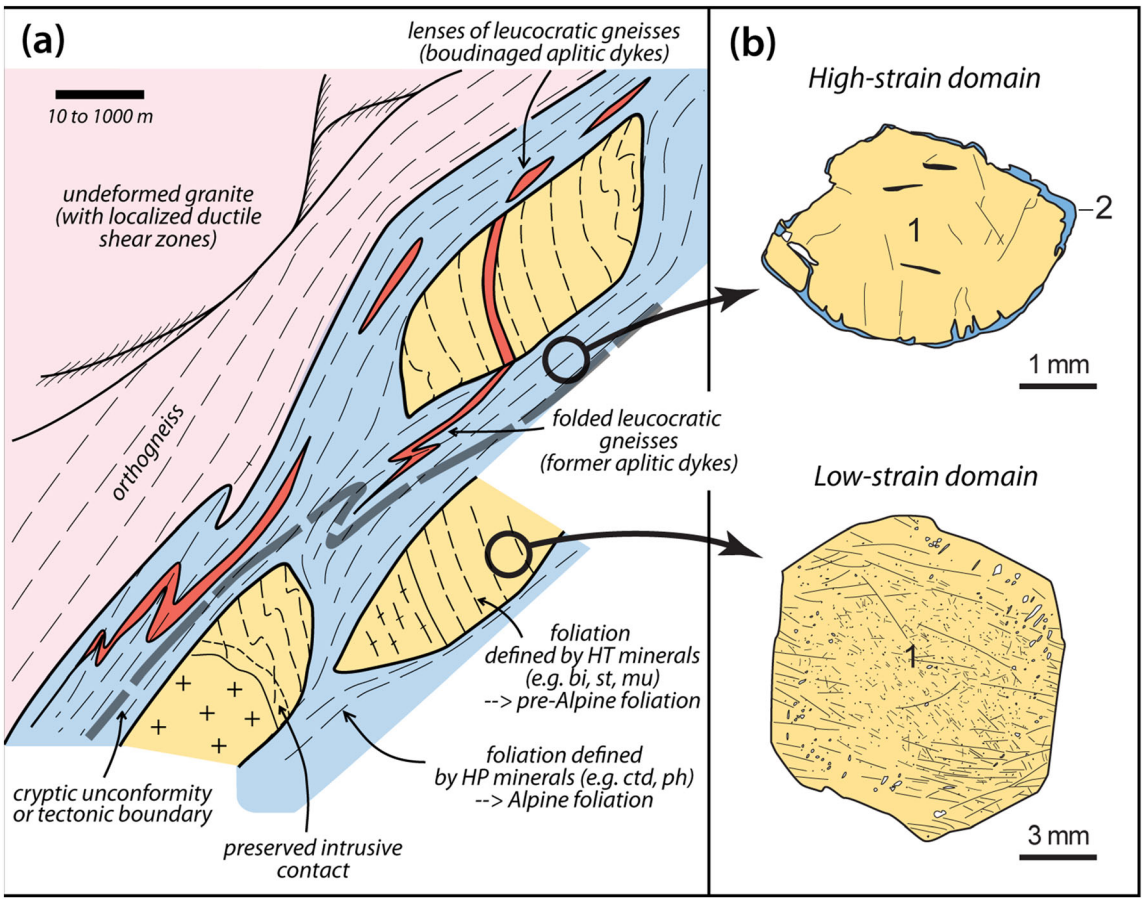

FIGURE 1 (a) Schematic representation of the strain patterns in a polycyclic basement. Low-strain volumes preserving structures and minerals from a first orogenic cycle (yellow) are bounded by rocks fully reworked during a second orogenic cycle (pale blue). (b) Garnet in low-strain domains may preserve their shape, inclusions, and chemical zoning, while garnet in the high-strain domains may display overgrowths related to the second orogenic cycle [Colour figure can be viewed at wileyonlinelibrary.com]

diorites (Bussy & Cadoppi, 1996; Manzotti et al., 2016; Novarese, 1895, 1898, 1905). This unit is comparable with the Money Unit in the Gran Paradiso Massif, in its similar structural position (i.e. the deepest unit in the Alpine nappe stack), age and types of sediments (Manzotti, Pitra, et al., 2015). In the Pinerolo Unit from the southern Dora-Maira Massif, Alpine peak *P*–*T* conditions have been estimated at 14–16 kbar 400–500°C (Avigad et al., 2003) and at 20–23 kbar and 500–515°C (Groppo et al., 2019).

Several tectonic units have been identified above the Pinerolo Unit in the southern Dora-Maira Massif, namely the San Chiaffredo, Brossasco-Isasca, Rocca Solei, and Dronero Units (e.g. Chopin et al., 1991; Compagnoni et al., 2012). By contrast, in its northern sector, a single tectonic unit (hereafter referred to as Muret Unit) has been described above the Pinerolo Unit (Borghi et al., 1996; Sandrone et al., 1993). In both sectors, the basement is dominated by Palaeozoic micaschist with minor metabasite and marble layers and it is intruded by Ordovician and Permian granitoids (Bussy & Cadoppi, 1996; Cadoppi, 1990; Cadoppi et al., 2016; Gebauer et al., 1997; Sandrone et al., 1993). Alpine metamorphism varies from blueschist-facies in the Dronero Unit, to quartz-eclogite in the Muret, San Chiaffredo and Rocca Solei Units, to coesite-eclogite in the Brossasco-Isasca Unit (Chopin et al., 1991; Compagnoni et al., 2012; Groppo et al., 2019; Michard et al., 1993). The coesite-eclogite metamorphism in the Brossasco-Isasca Unit is dated at ~35 Ma (based on U-Pb zircon and titanite geochronology; Gauthiez-Putallaz et al., 2016; Gebauer et al., 1997; Rubatto & Hermann, 2001; Xiong et al., 2021). The age of the high-pressure metamorphism in the other units is to date unknown.

2.2 | Pre-Alpine metamorphism in the Dora-Maira Massif

The Palaeozoic basement of the Dora-Maira Massif records pre-Alpine amphibolite to granulite facies conditions (Borghi et al., 1985; Bouffette et al., 1993; Compagnoni & Rolfo, 2003) that is heterogeneously

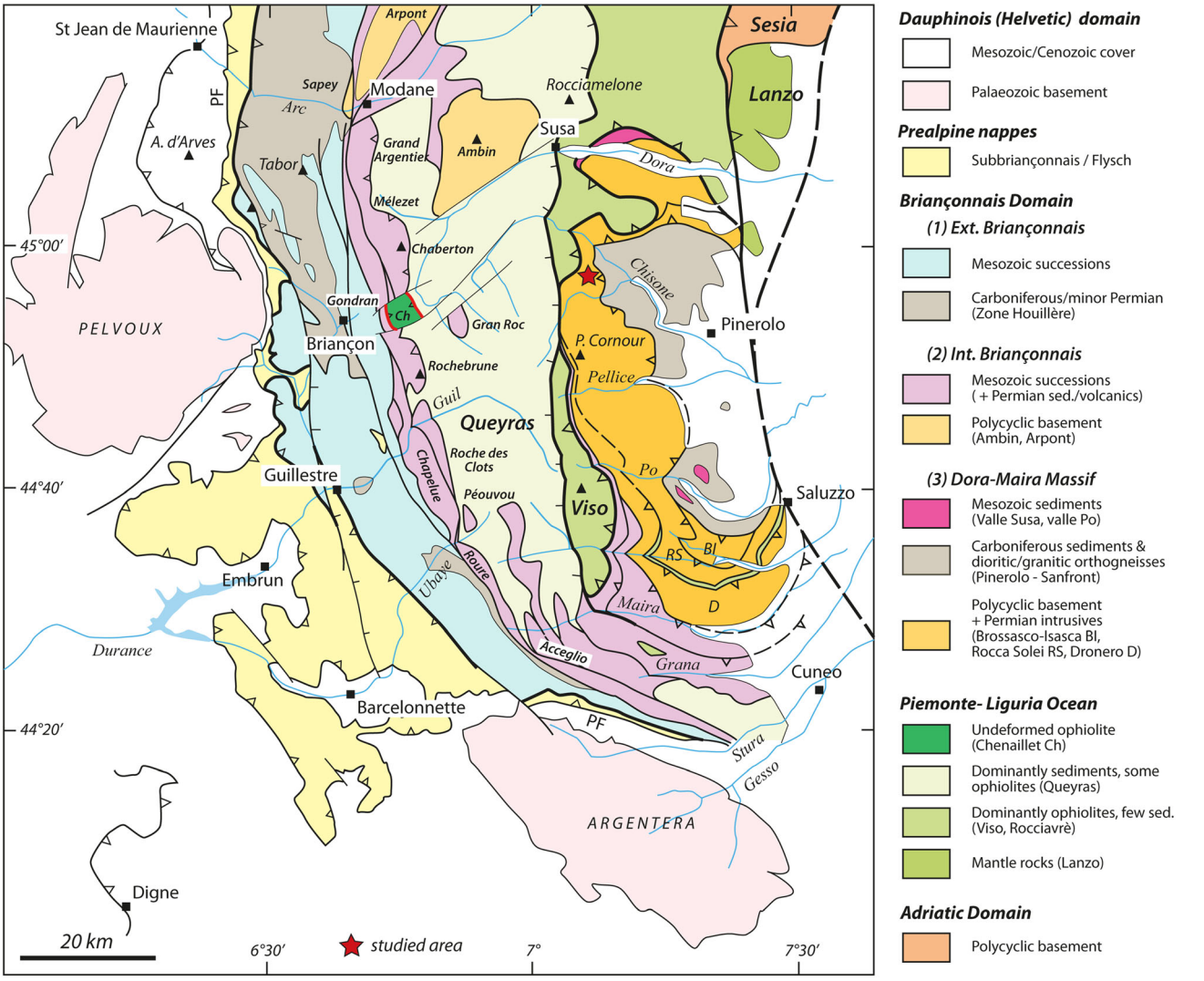

FIGURE 2 Simplified geological map of the SW Alps, showing the location of the studied area in the Dora-Maira Massif (modified after Ballèvre et al., 2020) [Colour figure can be viewed at wileyonlinelibrary.com]

preserved in domains that escaped pervasive Alpine overprint. In the micaschists, relicts of pre-Alpine metamorphism comprise garnet, muscovite, staurolite, sillimanite, and red-brown biotite (e.g. Cadoppi, 1990; Compagnoni & Rolfo, 2003). Pre-Alpine garnet is commonly surrounded by a second garnet generation Alpine in age (e.g. Gasco et al., 2011; Matsumoto & Hirajima, 2000; Sandrone & Borghi, 1992; Spiess et al., 2007). Staurolite and sillimanite are pseudomorphed by Alpine minerals (chloritoid and white mica on staurolite, Cadoppi, 1990; kyanite on sillimanite, Compagnoni & Rolfo, 2003). Red biotite is replaced by phengite ± rutile. Its pre-Alpine occurrence is also suggested by the abundant rutile needles included in Alpine garnet (e.g. Spiess et al., 2007).

Pseudomorphs after staurolite occur in the Muret Unit, Rocca-Solei and Dronero Units (Chopin et al., 1991; Groppo et al., 2019; Henry, 1990; Henry et al., 1993), whereas pseudomorphs after sillimanite have been reported from the Brossasco-Isasca Unit (Compagnoni et al., 1995; Compagnoni & Rolfo, 2003). In the Brossasco-Isasca Unit, leucocratic feldspar-rich domains have been interpreted as evidence of partial melting (Compagnoni et al., 1995; Compagnoni & Rolfo, 2003). In addition, polycyclic marbles from the Brossasco-Isasca Unit also display pre-Alpine relicts, such as garnet, diopside, olivine, and spinel (Castelli et al., 2007; Ferrando et al., 2017; Groppo et al., 2007). Relicts of pre-Alpine metamorphism are also locally found in Ordovician granodiorites, such as garnet-biotite-muscovite-plagioclase assemblages (Borghi et al., 1985; Bussy & Cadoppi, 1996). The amphibolite to granulite-facies metamorphism has been attributed to the Variscan orogeny (e.g. Cadoppi, 1990) although there are no radiometric data in support of this interpretation so far.

In the Brossasco-Isasca Unit, metapelitic xenoliths in Permian granitoids preserve evidence of contact metamorphism. In the metapelite the growth of biotite and muscovite and the replacement of pre-Alpine garnet by cordierite are attributed to the contact metamorphism (Compagnoni & Rolfo, 2003). In addition, aggregates of Alpine biotite and kyanite suggest the presence of pre-Alpine andalusite associated with contact metamorphism (Compagnoni et al., 1995; Compagnoni & Rolfo, 2003).

3 | METHODS

3.1 | Petrography and mineral chemistry

From about 30 samples representing the polycyclic basement, 3 samples preserving pre-Alpine mineralogy were selected for detailed investigation: a biotite orthogneiss (OG27) and 2 micaschists (GM1 and GM13). For each sample several polished thin sections were cut perpendicular to the main foliation and studied with the optical microscope, backscattered electron (BSE) images and the electron microprobe (details on the operating conditions are given in Appendix S1 in the supporting information). Representative chemical analyses of the main minerals are given in Tables S1–S3. Mineral abbreviations follow Holland and Powell (1998) and are listed in Appendix S2. Other symbols used are listed in Appendix S3.

3.2 | Bulk and local chemical compositions

The garnet micaschist samples (GM1 and GM13) display similar mineral assemblages but differ in grain size. Therefore, two different strategies were applied for estimating the system compositions used for phase diagram calculations. Sample GM1 displays heterogeneous grain size, with large garnet crystals (up to 2 cm in size) in a relatively fine-grained matrix (submillimetric to millimetric grain size). In order to obtain a representative bulk composition, we crushed a relatively large volume of rock and the whole rock composition of sample GM1 was obtained by X-ray fluorescence (XRF) on a fused glass chip. The crushed specimen was extracted from the hand sample as a representative volume of about 0.5 dm^3, avoiding veins and weathered surfaces. The homogeneous glass was obtained by fusion of a mixture of di-lithium tetraborate and rock powder in proportion of 5:2. XRF sample preparation and analyses were performed at the PetroTectonics analytical facility at Stockholm University.

Sample GM13 displays a homogeneous medium-fine grain size, with garnet up to a few millimetres large in a millimetre-size matrix. The effective bulk rock composition of this sample was obtained by area scan method using the scanning electron microscope equipped with energy dispersive spectrometer (SEM-EDS JSM-7100F at the University of Rennes 1). The chemical composition of six adjacent areas each 2 × 3 mm in size was analysed and averaged (e.g. Groppo et al., 2006; Groppo, Beltrando, et al., 2009; Groppo, Rolfo, et al., 2009; Manzotti, Bosse, et al., 2018; Manzotti, Poujol, et al., 2015), in order to obtain a representative local chemical composition. The total area includes a garnet crystal that is studied in detail (see Section 5 for further details). The bulk composition (major elements) of the biotite orthogneiss (sample OG27) was obtained by XRF, using the same method applied to sample GM1. All the bulk composition obtained for the three samples investigated are listed in Table S4.

3.3 | *P–T* modelling

For the two micaschists (GM1 and GM13), *P–T* pseudosections were calculated with Theriak-Domino (De Capitani & Brown, 1987; De Capitani & Petrakakis, 2010) and the internally consistent thermodynamic dataset 5.5 (Holland & Powell, 1998; updated November 2003, converted for Theriak/Domino by D.K. Tinkham). Phase relations were modelled in the chemical system MnO-Na_2O-CaO-K_2O-FeO-MgO-Al_2O_3-SiO_2-H_2O-TiO_2-Fe_2O_3 (MnNCKFMASHTO). The phases considered in the calculations and the activity compositions models used are plagioclase (Holland & Powell, 2003), garnet, biotite, ilmenite (White et al., 2005), chlorite (Mahar et al., 1997), muscovite (Coggon & Holland, 2002), magnetite (White et al., 2000), epidote, cordierite, staurolite, chloritoid (Holland & Powell, 1998), amphibole, clinopyroxene (Diener & Powell, 2012), carpholite (Wei & Powell, 2004), melt (White et al., 2007), andalusite, sillimanite, kyanite, albite, rutile, titanite, and quartz. Water was considered in excess. The fraction of ferric iron was set to 5 wt.% of the total iron, an arbitrary low value considered accurate in a pelitic chemical system (e.g. Manzotti, Bosse, et al., 2018). In sample GM1, apatite is present. Thus, for this sample the amount of Ca was corrected for the presence of apatite. In sample GM13, monazite occurs in the areas scanned by SEM-EDS. Apatite is not present in these domains. Therefore, the amount of Ca was corrected for the presence of monazite.

Additional constraints on the *P–T* evolution of sample GM13 were obtained with the garnet-ilmenite thermometer (Table S5) based on the Fe-Mn ion exchange (experimental calibration by Pownceby et al., 1991).

3.4 | Mineral separation and zircon and monazite geochronology

Zircon crystals were separated from an orthogneiss (sample OG27) and two micaschists (samples GM1 and GM13) from the Muret Unit at Stockholm University. About 1.5 dm^3 of sample was crushed and milled with a Resch PM400 tungsten steel mortar, obtaining a powder with heterogeneous grain size (from grains smaller than 100 μm to grains up to 1 mm large). Zircon grains were separated using a Wilfley Table, handpicked, mounted on a one-inch epoxy resin puck and polished to expose the equatorial section. Particular attention was paid to the micaschist samples (GM1 and GM13) in selecting grains with different size, shape, and colour, in order to avoid handpicking biases in a zircon population (Sláma & Košler, 2012). The zoning of the selected grains was studied by cathodoluminescence (CL) imaging using an XL30 ESEM-FEG equipped with a Centaurus detector (15-kV accelerating voltage) at the Swedish Museum of Natural History (NRM).

U-Th-Pb ages and trace element compositions of monazite (sample GM1) were analysed in microtextural context (thin section). Monazite internal texture was studied by BSE imaging using an ESEM FEI Quanta FEG 650 (20-kV accelerating voltage) at the Swedish Museum of Natural History (NRM).

U-(Th)-Pb geochronology of zircon and monazite was performed by in situ LA-ICP-MS using a GeOHeLiS analytical platform (University of Rennes 1, France) with an ESI NWR193UC Excimer laser coupled to an Agilent quadrupole 7700x ICP-MS. The instrument working conditions are reported in Appendix S4 and S5 for zircon and monazite, respectively. Ablation spot diameters of 25 and 20 μm with repetition rate of 5 Hz and fluence of 6.2 J/cm^2 were used for zircon, whereas spot diameters of 8 μm with repetition rate of 5 Hz and fluence of 6.5 J/cm^2 were used for monazite. Data were corrected for U-(Th)-Pb fractionation and mass bias by standard bracketing with repeated measurements of the GJ1 zircon reference material (Jackson et al., 2004) and Moacyr monazite reference material (Gasquet et al., 2010). Along with the unknowns, the Plešovice standard zircon (Sláma et al., 2008) and Manangoutry standard monazite (Paquette & Tiepolo, 2007) were measured to monitor precision and accuracy of the analyses and produced concordia ages of 339.4 ± 1.7 Ma (95% c.i.; $MSWD_{(concordance + equivalence)} = 1.2$; $n = 18$) and 554 ± 18 Ma (95% c.i.; $MSWD_{(concordance + equivalence)} = 0.59$; $n = 5$), respectively. Data processing was carried out with the software Iolite v4 (Paton et al., 2010; Paton et al., 2011). The reproducibility of the quality control reference material Plešovice and Manangoutry has been propagated by quadratic addition for the individual analyses reported in Tables S6–S9 (Horstwood et al., 2016). Concordance was calculated as follows: If $Age^{206}Pb/^{238}U < 1000$ Ma, then conc % = ($Age^{206}Pb/^{238}U/Age^{207}Pb/^{235}U$) * 100; else conc % = ($Age^{207}Pb/^{235}U/Age^{207}Pb/^{206}Pb$) *100. Concordance for detrital and inherited zircon dates is accepted if 90%–105% concordance and for magmatic and metamorphic zircon and monazite dates if 97–102% concordance. The complete dataset is provided in Table S6–S9. Mean ages, concordia ages, and diagrams were generated with IsoplotR (Vermeesch, 2018). In the text, individual analyses are presented as $^{206}Pb/^{238}U$ dates with 2σ errors, whereas weighted mean ages and concordia ages are given at the 95% confidence level. Mean squared weighted deviations (MSWD) are given for concordance plus equivalence.

In order to get the most precise and accurate measurements for age and trace element content, two types of analytical session were carried out. In the first session, we only measured the age whereas during the second session trace element contents were measured. In zircon both the ages and the trace element contents were measured. This allowed us to be sure that the trace element contents were measured in the right domain within each grain, especially for the zircon rims that are relatively narrow. For the age calculations, however, only the data acquired during the first sessions (i.e. without trace element measurements) were used as they were more precise.

3.5 | Zircon, garnet, and monazite trace element geochemistry

Zircon, garnet, and monazite trace element concentrations were acquired in situ by LA-ICP-MS in the GeOHeLiS analytical platform (University of Rennes 1, France) using an ESI NWR193UC Excimer laser coupled to an Agilent quadrupole 7700x ICP-MS. Laser spots for zircon, garnet, and monazite analyses were 25, 60, and 8 μm in diameter, respectively. Repetition rate of 4 Hz and fluence of 5.8 J/cm^2 were used for zircon, 4 Hz and 5.7 J/cm^2 were used for garnet, and 5 Hz and 6.5 J/cm^2 were used for monazite. NIST-612 synthetic glass was used as primary standard for zircon and monazite, whereas NIST-610 was used for garnet. Internal standardization was to SiO_2 for zircon and garnet (17.73% for zircon and 37% for garnet) and to ^{140}Ce with a value of 247,615 ppm for monazite. Data processing was carried out with the software Iolite v4 (Paton et al., 2011) and its data reduction scheme for trace elements (Woodhead et al., 2007). Rare earth elements (REE) patterns were normalized to chondrite (McDonough & Sun, 1995). The

analytical datasets for zircon, garnet, and monazite are provided in Table S10–S13.

4 | THE ORTHOGNEISS AND POLYCYCLIC MICASCHIST OF THE PUNTA MURET

In the northern sector of the Dora-Maira Massif, the Muret Unit is well exposed in the Punta Muret area on the ridge between the Chisone and Germanasca valleys. This area covers approximatively 3 km^2 and comprises the summit of the Punta Muret (2,210 m) and its southern slope up to the Alpe Muret (1,843 m). The polycyclic basement of the Dora-Maira Massif here comprises a kilometre-scale low-strain domain of spectacular garnet-staurolite micaschist and a biotite orthogneiss (hereafter called the Muret orthogneiss) (Bouffette et al., 1993; Cadoppi, 1990; Novarese, 1895; Vialon, 1966). These lithologies display evidence of pre-Alpine deformation and amphibolite-facies metamorphism, as the Alpine overprint is heterogeneous and mainly localized in the micaschist. Garnet-micaschist with a dominant Alpine fabric and paragenesis occurs outside the low-strain domain.

The *Muret orthogneiss* is a medium-grained augen gneiss that crops out as a lenticular body (~300 m thick and ~2 km long) along the southern slope of the Punta Muret. The rock contains biotite, muscovite and minor garnet (1–5 mm in size; Figure 3a) as a pre-Alpine metamorphic assemblage. Biotite and white mica also define a pre-Alpine metamorphic foliation that wraps around the stretched alkali feldspar porphyroclasts (1–2 cm in size; Figure 3b) and microgranular mafic enclaves. The latter are centimetre to decimetre in size, of lenticular shape (Figure 3c,d) and consist of biotite and minor fine-grained feldspars. The contact between the Muret orthogneiss and garnet-staurolite micaschist is parallel to the pre-Alpine foliation observed in both lithologies. The proportion of alkali feldspar porphyroclasts progressively decreases towards the contact with the garnet-staurolite micaschist, along a band ~2 m thick.

Garnet-staurolite micaschist displays heterogeneous grain size, with large euhedral pre-Alpine garnet porphyroblasts, pseudomorphed staurolite and a fine-grained quartz- and white mica-rich matrix. A pre-Alpine foliation is defined by the alternation of quartz- and mica-rich layers (0.3–1.5 cm thick) and by the shape preferred orientation of white mica (Figure 4a,b). Garnet (1–3 cm in size) is wrapped by the pre-Alpine foliation. Quartz pressure shadows are common around garnet (Figure 4a,b). Dark green fine-grained aggregates of chloritoid and white mica, parallel to the pre-Alpine foliation, pseudomorph staurolite, and locally display prismatic crystallographic faces (Figure 4c).

Veins and nodules (1–5 cm in size) of tourmaline and quartz are locally found near the Muret orthogneiss and are rotated parallel to the pre-Alpine foliation (Figure 4a,b). Alpine deformation results in the crenulation of the pre-Alpine foliation (Figure 4a) and local development of a new axial plane foliation. The Alpine overprint is very weak near the Muret orthogneiss and becomes progressively more intense away from the magmatic body. Pseudomorphs after staurolite are strongly deformed ~100 m from the Muret orthogneiss: They occur as lenticular dark domains and their prismatic crystallographic faces are no longer recognizable.

Garnet micaschist shows a fine grain size and crops out on the Punta Muret ridge. It is grey in colour due to the presence of graphite and contains tiny (1–3 mm in size) subhedral garnet crystals (Figure 4d). The main foliation is Alpine, defined by the shape preferred orientation of white mica that wraps around garnet and is oriented at high angle with respect to the pre-Alpine foliation of the Muret orthogneiss and garnet-staurolite micaschist.

5 | PETROGRAPHY AND MINERAL CHEMISTRY

Three samples have been studied in detail: the Muret orthogneiss (OG17), a garnet-staurolite micaschist (GM1), and a garnet micaschist (GM13).

5.1 | Muret orthogneiss (OG27)

Sample OG27 is a medium-grained garnet-biotite orthogneiss collected a few metres structurally above the contact with the micaschist GM1 (Lat/Long coordinates 44°57′39.59” N – 7°6′11.29″ E). The rock consists of plagioclase (~30%), quartz (~25%), biotite (~15%), alkali feldspar (~10%), muscovite (~10%), garnet (<5%), epidote (<5%), chlorite (<5%), and accessory apatite, ilmenite, titanite, and zircon. The protolith of the orthogneiss was a peraluminous granodiorite (A/CNK = 1.28), with low total alkali content ($K_2O + Na_2O$ = 6.95 wt.%; Table S4). This pre-Alpine granodiorite then underwent amphibolite-facies metamorphism, followed by a late greenschist-facies retrogression, the age of which is difficult to ascertain (Figure 5a). The pre-Alpine igneous minerals are porphyroclastic alkali feldspar, quartz, apatite, allanite, and zircon, whereas the pre-Alpine metamorphic assemblage comprises biotite, muscovite, plagioclase, garnet, ilmenite, and clinozoisite. The shape

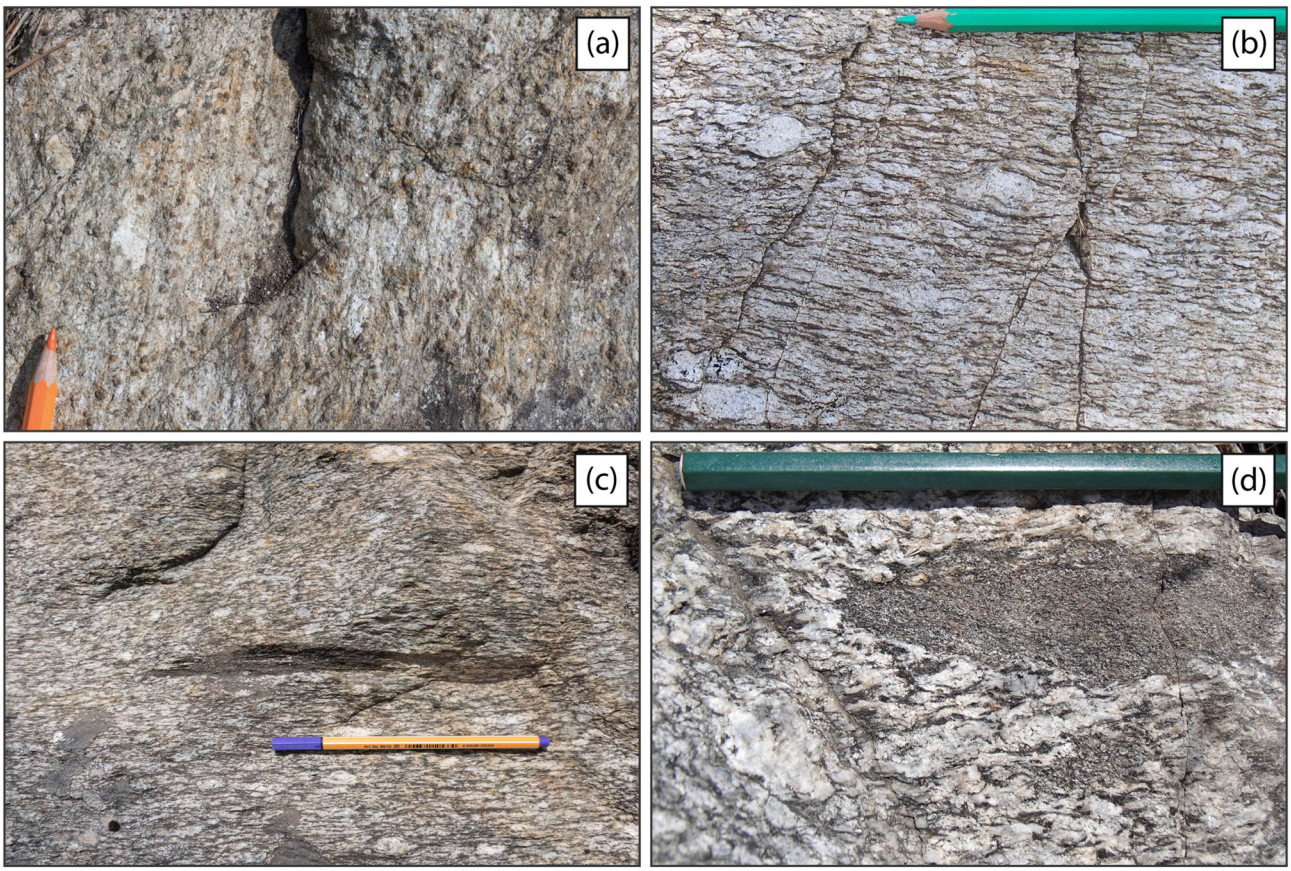

FIGURE 3 Field photographs of the Muret orthogneiss. (a) Garnet, up to 5 mm in size, dispersed in the Muret orthogneiss. (b) Orthogneiss with a pre-Alpine metamorphic foliation defined by the preferred orientation of biotite and white mica. Alkali feldspar porphyroclasts are elongated parallel to the pre-Alpine metamorphic foliation. (c) Highly stretched mafic enclave oriented parallel to the pre-Alpine metamorphic foliation. (d) Lenticular-shaped mafic enclave consisting of fine-grained biotite and minor feldspars [Colour figure can be viewed at wileyonlinelibrary.com]

preferred orientation of biotite ($X_{Fe} = 0.62–0.66$, Ti = 0.08–0.16 a.p.f.u.), muscovite (Si = 3.17–3.24 a.p.f.u., $X_{Na} = 0.03–0.04$), and ilmenite (~100 μm in size) define a pre-Alpine metamorphic foliation, wrapping around magmatic feldspar. Plagioclase crystals (0.5–1.5 mm in size) are slightly elongated parallel to this fabric. Plagioclase is zoned oligoclase with a calcic core (An = 24–29%) and more sodic rim (An = 18–20%); and contains inclusions of quartz, microcline (Or = 94%), muscovite (Si = 3.21 a.p.f.u.), and apatite. Microcline (~1 mm in size; Or = 93%–94%) contains muscovite inclusions (Si = 3.23–3.24 a.p.f.u.). Garnet (0.5–0.8 mm in size) contains quartz inclusions and has a rather homogeneous composition in grossular (19–22 mol.%) and pyrope (4 mol.%). Spessartine (3–14 mol.%), almandine (46–55 mol.%), and andradite (2–8 mol.%) contents vary irregularly from core to rim. Clinozoisite forms rims around magmatic allanite and is oriented parallel to the foliation. During the late greenschist-facies stage, garnet is pervasively fractured and replaced by chlorite ($X_{Fe} = 0.65–0.67$) and minor pale brown biotite (Ti = 0.2 a.p.f.u., $X_{Fe} = 0.65$) (late stage in Figure 5a). Chlorite ($X_{Fe} = 0.61–0.64$) also replaces biotite along its edges. Titanite partially replaces ilmenite. Fractures are filled by chlorite, quartz and minor albite.

5.2 | Garnet-staurolite micaschist (GM1)

Sample GM1 is a micaschist collected on the unsealed road to the Alpe Muret (Lat/Long coordinates 44°57′37.02″N to 7°6′12.01″E), a few metres structurally below the contact with the Muret orthogneiss body. It displays a heterogeneous grain size and contains garnet (~25%), quartz (~30%), white mica (~25%), chloritoid (~15%), chlorite (<5%), and accessory rutile, ilmenite, albite, epidote, apatite, monazite, and zircon.

The rock preserves mineralogical and structural relicts of the pre-Alpine evolution with an incomplete re-equilibration during the Alpine cycle (Figure 5b). A

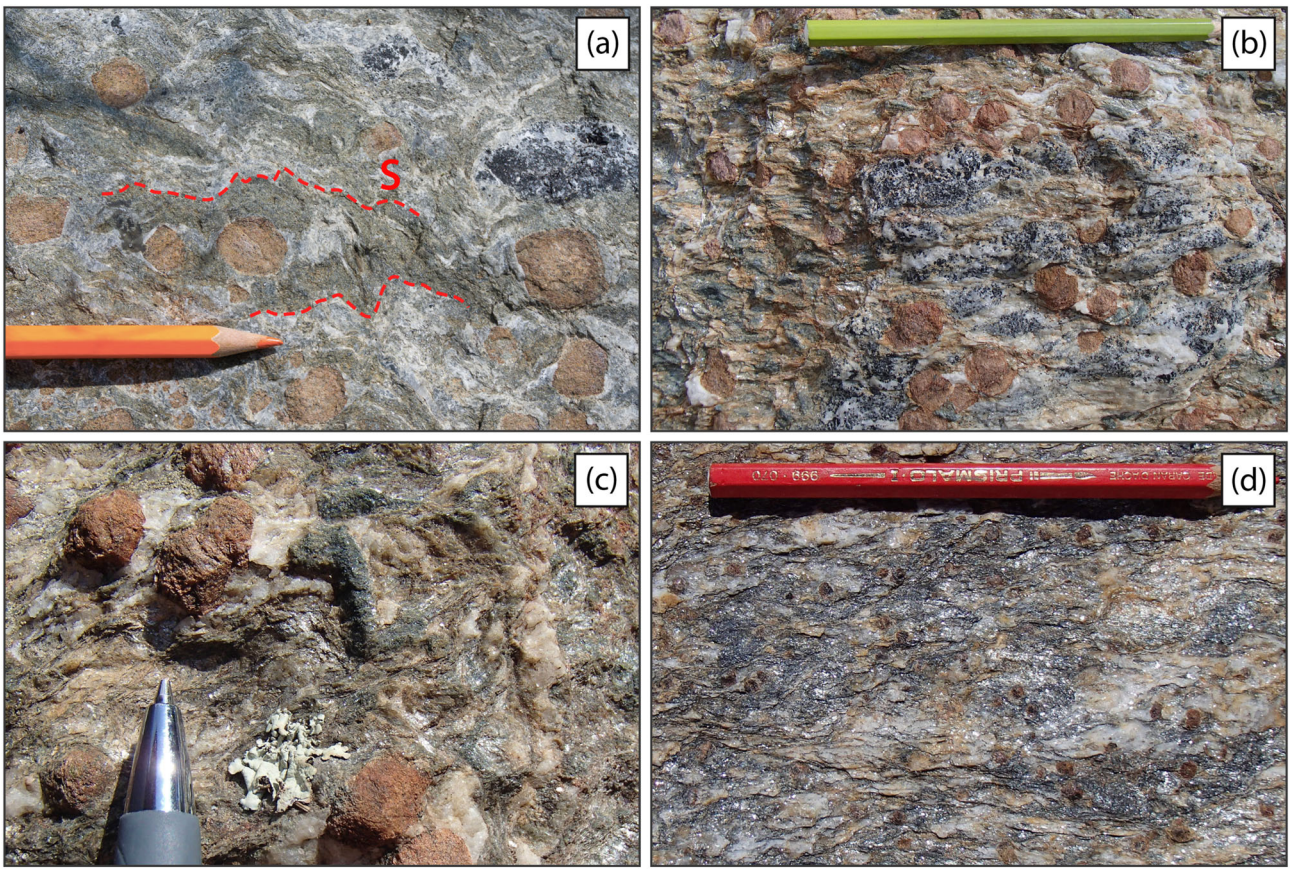

FIGURE 4 Field photographs of garnet-staurolite micaschist (a–c) and garnet micaschist (d) of the Punta Muret Unit. (a) Micaschist displays pre-Alpine garnet porphyroblasts and a pre-Alpine foliation defined by the alternation of quartz- and mica-rich layers (marked by red dashed lines). This structure is crenulated during the Alpine evolution. At the top right corner of the photograph are cm-sized veins and nodules of tourmaline and quartz. (b) Tourmaline-quartz veins oriented parallel to the pre-Alpine foliation. (c) Pseudomorph after staurolite with preserved prismatic crystallographic faces. (d) Grey-coloured garnet micaschist cropping out outside the low-strain domain [Colour figure can be viewed at wileyonlinelibrary.com]

pre-Alpine foliation is defined by the alternation of mica-rich layers (1–10 mm thick) and quartz-rich layers (0.5–1.5 cm thick) and by the preferred orientation of low-Si muscovite (Si = 3.07–3.11 a.p.f.u., X_{Na} = 0.20–0.27). Elongated mm-sized domains consisting of fine-grained aggregates of chloritoid (X_{Fe} = 0.79–0.81), paragonite (X_{Na} = 0.92–0.94), high-Si muscovite (Si = 3.37–3.42 a.p.f.u., X_{Na} = 0.03–0.05), and ilmenite are observed in the matrix as well as in garnet rims (Figure 6a,b,c). In the matrix, these domains are oriented parallel to the pre-Alpine foliation and may represent pseudomorphs after pre-Alpine staurolite, as described in the pre-Alpine basement of the Grand Saint Bernard (Burri, 1983; Thélin, 1992), Gran Paradiso (Le Bayon et al., 2006), and the Dora-Maira Massif (Cadoppi, 1990; Chopin et al., 1991). Centimetre-sized euhedral garnet porphyroblasts, strongly fractured and partially wrapped by the pre-Alpine foliation (Figure 6d), are interpreted to be pre-Alpine. Garnet is zoned with a core (zone A), mantle (zone B) and rim (zone C). In hand sample garnet cores and mantles have orange colour (sometimes garnet mantles appear darker than the core) whereas garnet rims have a reddish colour. Inclusions of muscovite, ilmenite (commonly pervasively replaced by fine-grained rutile), and quartz are mainly observed in garnet cores (zone A). Aligned quartz inclusions in garnet cores (zone A) and mantles (zone B) define an internal foliation (locally gently folded) that may be concordant or discordant with the external matrix foliation (Figure 6c). Tiny (from a few microns up to 20 μm) anhedral zircon and apatite (5 to 50 μm in size) occur in garnet cores (zone A, Figure S1), whereas larger monazite crystals (up to 200 μm in size) appear first in garnet mantles (zone B) and become more abundant in garnet rims (zone C, Figure S1). Chemical zoning in garnet is characterized by a core-to-rim decrease in grossular (from 21 to 3 mol.%) and spessartine (from 15 to 1 mol.%), compensated by an increase in almandine (from 57 to 82 mol.%) and pyrope

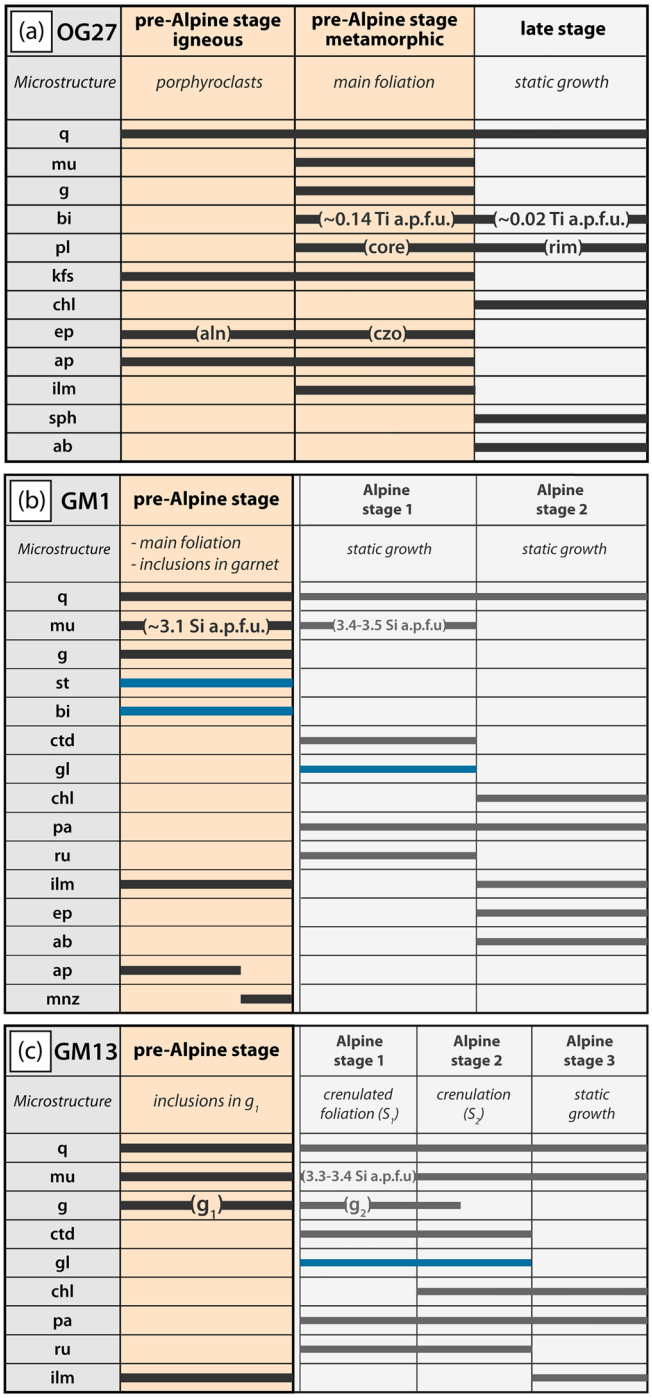

FIGURE 5 Deformation/mineral growth relationships (only observed or pseudomorphed minerals) for the (a) Muret orthogneiss OG27, (b) garnet-staurolite micaschist GM1 and (c) garnet micaschist GM13. The blue line indicates pseudomorphed minerals [Colour figure can be viewed at wileyonlinelibrary.com]

(from 4 to 23 mol.%; Figure 7a). X_{Fe} decreases from 95% to 86% from core to rim (Figure 7a). Distinctive Y oscillations are observed in garnet (Figure 7b). Y is enriched (~250 ppm) in the cores (coreward of zone A), decreases outwards, then increases (up to 1,000 ppm) again in the centre of garnet mantles (zone B) and finally decreases in garnet rims (~100 ppm, zone C; Figure 7b). The zoning of Y commonly parallels the Zr and Hf patterns (especially in zone B; Figure 7c). The Y increase also corresponds to HREE- and MREE-enriched domains (Figure 7b). An increase in P is observed from zone B to zone C (up to ~750 ppm; Figure 7d). Garnet rims (zone C) also display a small but distinct negative Eu anomaly ($Eu/Eu_* = 0.31–0.77$; Figure 7e). The low-Y rims (zone C) also correspond to the low-Ca and Mn contents observed in the major element profile (Figure 7a and Table S11).

A *HP* mineral assemblage consisting of high-Si muscovite, paragonite, chloritoid, glaucophane (never preserved but pseudomorphed), and rutile developed during the Alpine cycle (Alpine stage 1, Figure 5b). High-Si muscovite (Si = 3.37–3.50 a.p.f.u., $X_{Na} = 0.01–0.07$) overgrows concentrically pre-Alpine muscovite (Figure S2) or forms new crystals. The latter display numerous tiny rutile crystals and may be derived from pre-Alpine biotite. Paragonite ($X_{Na} = 0.92$) and chloritoid (~300 μm in size) are postkinematic with respect to the pre-Alpine foliation. Sample GM1 does not display a second generation of garnet. By contrast, tiny (50 to 100 μm in size) idioblastic garnet crystals have been observed in sample GM2 collected in the same area. Chloritoid shows chemical zoning, with increasing Fe content from the core ($X_{Fe} = 0.70–0.71$) to rim ($X_{Fe} = 0.73–0.79$). Fine-grained elongated or lozenge-shaped aggregates of chlorite are interpreted as pseudomorphs after sodic amphiboles, as reported in other Alpine units with similar metamorphic evolution (Compagnoni, 1977; Manzotti et al., 2021). Rutile occurs in the matrix as tiny needles and as large crystals (maximum 100 μm in length). During a second Alpine stage (Alpine stage 2; Figure 5b) chlorite statically grows in the matrix and replaces garnet whereas ilmenite forms coronas around rutile. Paragonite, rare albite, and epidote also grow during this stage.

5.3 | Garnet micaschist (GM13)

Sample GM13 is a micaschist collected at the summit of the Punta Muret (Lat/Long coordinates 44°58′10.54″N to 7°6′26.38″E). The rock displays a rather homogeneous grain size and consists of garnet (~15%), white mica (~35%), quartz (~30%), chlorite (~10%), chloritoid (<5%), graphite (<5%), and accessory rutile, ilmenite, zircon, and monazite.

This rock preserves evidence of a polycyclic evolution comprising a pre-Alpine and three Alpine stages (Figure 5c).

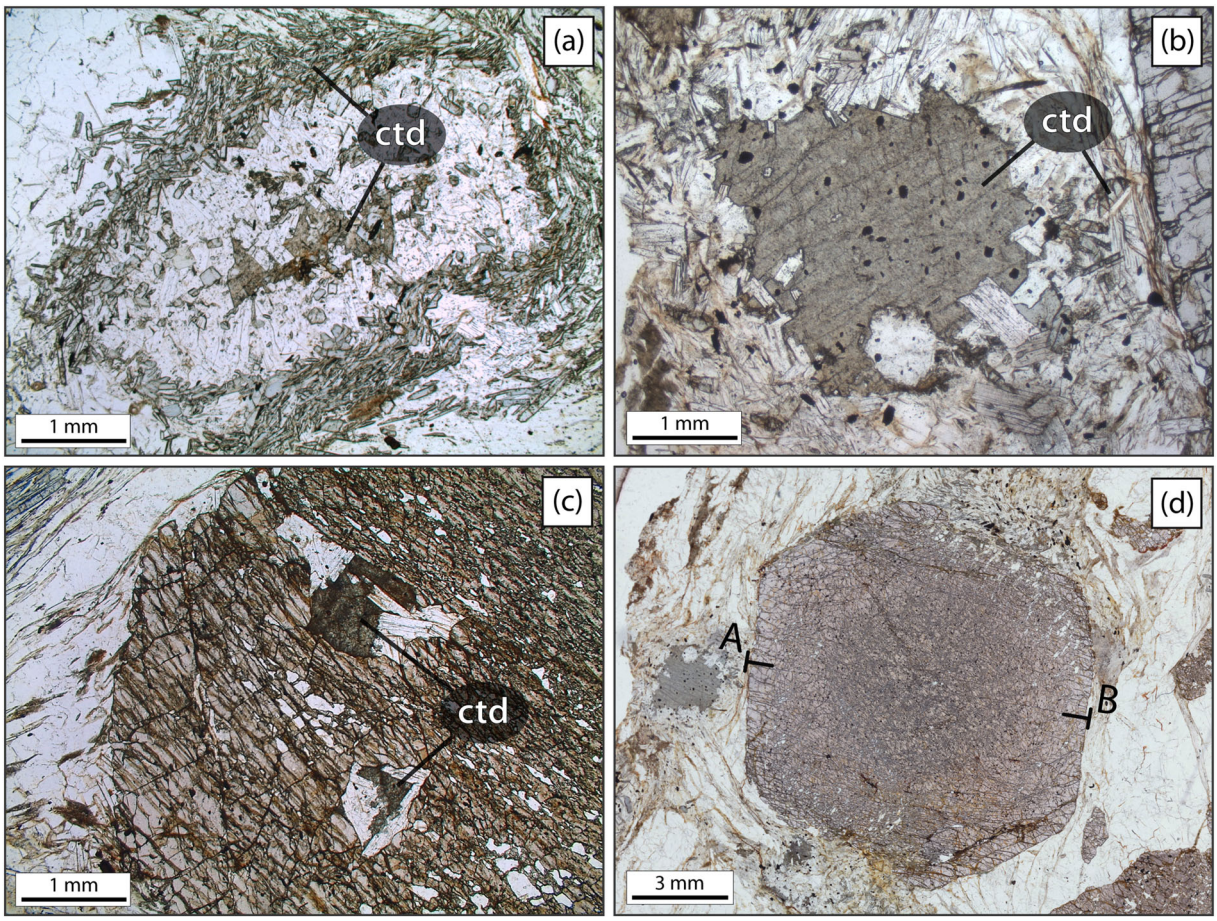

FIGURE 6 Thin section photomicrographs for sample GM1 (PPL). (a, b) Pseudomorphs after staurolite, consisting of a fine-grained chloritoid aggregate surrounded by white mica + chloritoid and a cluster of chloritoid. (c) Pseudomorph after staurolite included in garnet rim. Garnet rim preserves an internal foliation mainly defined by elongate quartz inclusions and oriented at high angle with respect to the matrix foliation. (d) Centimetre-sized pre-Alpine garnet porphyroblast. The A-B markers indicate the position of the compositional profile in Figure 7a [Colour figure can be viewed at wileyonlinelibrary.com]

The pre-Alpine stage consists of a first generation of garnet ($garnet_1$), which has inclusions of ilmenite, quartz, muscovite, and graphite. $Garnet_1$ (1–5 mm in size) is wrapped by the Alpine foliation and locally is irregularly shaped with embayment, suggesting partial dissolution and resorption (Figure 8a,b). Inclusions of ilmenite (up to 500 μm long; Figure 8b) and quartz (up to 200 μm large) are found in $garnet_1$ cores and locally define an internal foliation discordant to the main matrix foliation. Ilmenite included in $garnet_1$ is partially or completely replaced by fine-grained aggregates of Alpine rutile. Along resorbed edges, $garnet_1$ is locally cloudy due to the presence of micro-inclusions (graphite, muscovite, quartz, zircon, and rutile) (Figure 8b). $Garnet_1$ displays a chemical zoning (Figures 7f and 8c–f) characterized by a decrease in grossular (from 12 to 2 mol.%) and spessartine (from 32 to 1 mol.%) from core to rim, compensated by an increase in almandine (from 50 to 79 mol.%) and pyrope (from 3 to 15 mol.%). In detail, grossular content displays a plateau and a slight increase (from 12 to 14 mol.%) in the cores, whereas spessartine continuously decreases (from 32 to 12 mol.%).

A second generation of garnet ($garnet_2$) forms a thin (up to 30 μm) and discontinuous overgrowth around $garnet_1$ (indistinctly along preserved or resorbed edges) and seals fractures within $garnet_1$ (Alpine stage 1). The transition between $garnet_1$ and $garnet_2$ is sharp and corresponds to a decrease in almandine (from 79 to 68 mol.%) and pyrope (from 15 to 10 mol.%) and an increase in grossular (from 3 to 14 mol.%). Spessartine content does not display a variation from $garnet_1$ rim to $garnet_2$ (1 mol.%) (Figures 7f and 8c–f).

An early microfolded schistosity S_1 (Alpine stage 1) is partially transposed by the main foliation S_2 (Alpine stage 2). S_1 foliation is defined by discontinuous millimetre-thick quartz layers and by the shape preferred orientation of white mica, chloritoid, and graphite. Pressure shadows around garnet contain

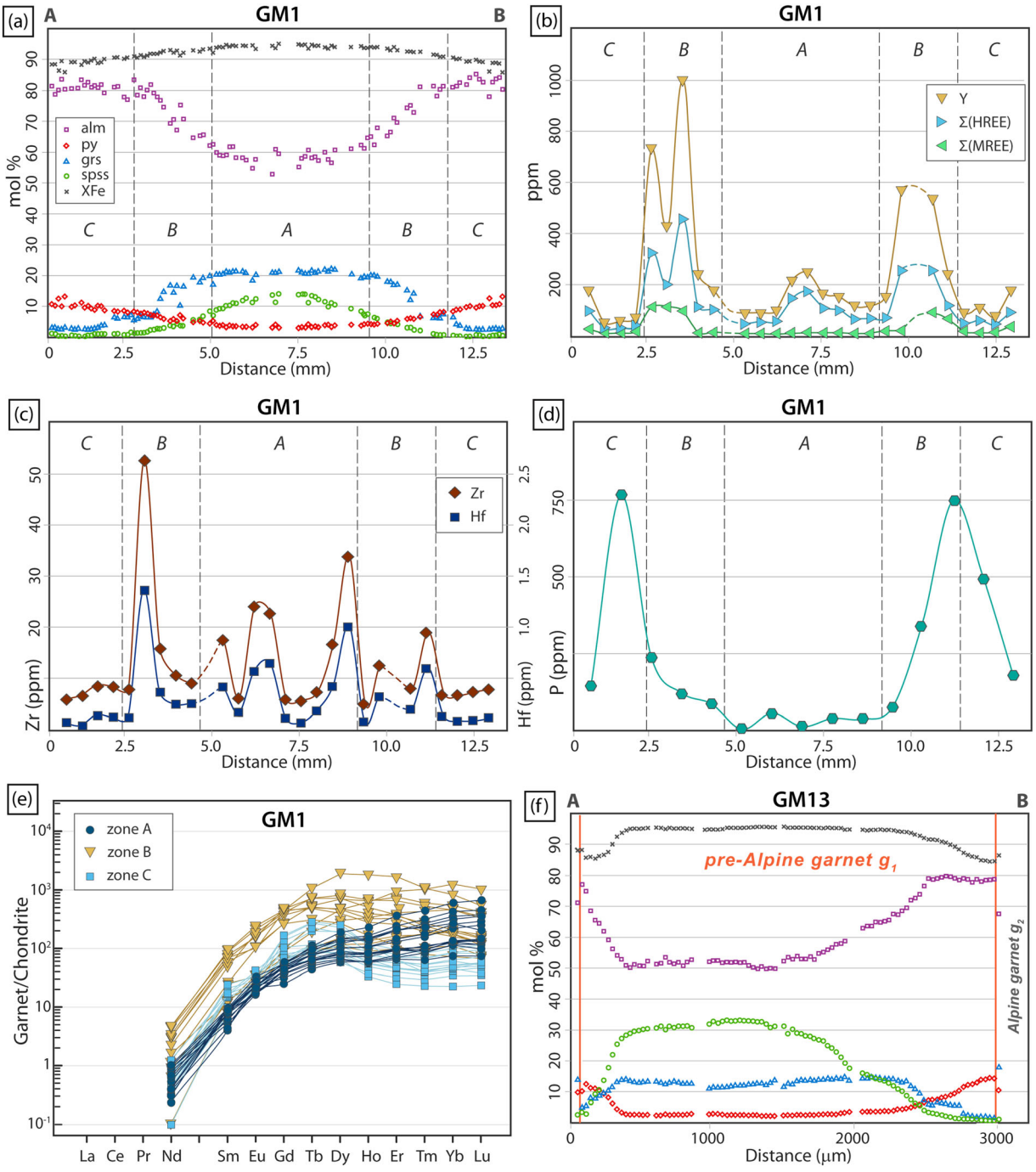

FIGURE 7 Compositional profile of pre-Alpine garnet from garnet-staurolite micaschist (GM1) for major (a) and trace elements (b–d). (b) Compositional profile of Y and sum of HREE and MREE. (c) Compositional profile of Zr and Hf. (d) Compositional profile of P. (e) Chondrite-normalized REE pattern (McDonough & Sun, 1995) for pre-Alpine garnet in sample GM1. (f) Compositional profile of polycyclic garnet from garnet micaschist (GM13) (colour coding as in (a)). Vertical orange lines mark the boundaries between the first and second garnet generations. The position of the profiles (a) and (f) is indicated in Figure 6d and Figure 8e, respectively (lines A-B) [Colour figure can be viewed at wileyonlinelibrary.com]

quartz, white mica, and rutile. White mica consists of Si-rich muscovite (Si = 3.3–3.4 a.p.f.u., X_{Na} = 0.02–0.06) and minor paragonite (X_{Na} = 0.90–0.92). A few elongated or lozenge-shaped domains (up to 2 mm large), wrapped by the S_2 foliation or oriented parallel to it, consist of fine-grained chlorite, quartz, and albite. These domains are interpreted as pseudomorphs after sodic amphiboles, similar to those observed in sample GM1.

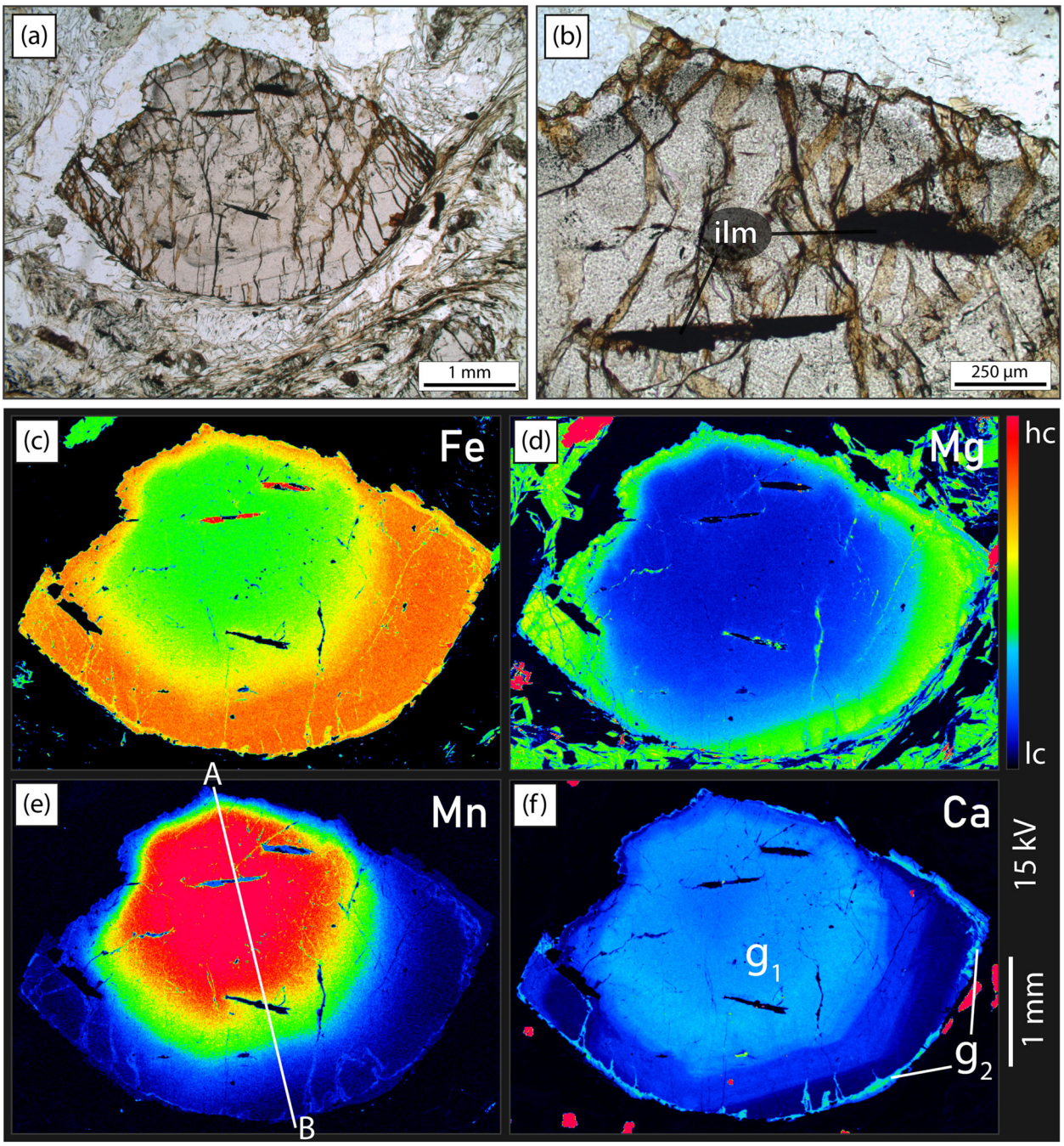

FIGURE 8 Thin section photomicrographs (PPL) and X-ray maps of a polycyclic garnet from the garnet micaschist GM13. (a) Photomicrograph of polycyclic garnet wrapped by the main Alpine foliation. Garnet is partially dissolved and displays resorbed edges on one side. (b) Ilmenite included in $garnet_1$ is partially replaced by fine-grained rutile. Along this resorbed edge, $garnet_1$ is "cloudy" due to the presence of micro-inclusions of graphite, quartz, muscovite and zircon. (c) Fe X-ray map of the garnet shown in (a, b). Ilmenite inclusions in $garnet_1$ are only partially preserved (lc = low concentration; hc = high concentration). (d) Mg X-ray map. (e) Mn X-ray map. The A-B trace indicates the position of the compositional profile in Figure 7f. (f) Ca X-ray map showing a sharp chemical discontinuity between two garnet generations. Alpine $garnet_2$ forms a thin and discontinuous overgrowth over the partially dissolved pre-Alpine $garnet_1$ [Colour figure can be viewed at wileyonlinelibrary.com]

Rutile (<100 µm in size) is aligned with the S_1 and S_2 foliation (Alpine stages 1 and 2), and it is locally overgrown by Alpine ilmenite (Alpine stage 3). Chlorite (X_{Fe} = 0.45–0.49) is oriented parallel to the S_2 foliation and replaces garnet along fractures (Alpine stages 2 and 3, respectively). Postkinematic paragonite

($X_{Na} = 0.93–0.94$) grows over the S_2 foliation (Alpine stage 3).

6 | RESULTS

6.1 | *P–T* conditions

The chemical zoning of pre-Alpine garnet and its inclusions (e.g. ilmenite, muscovite, and quartz) were used to model the pre-Alpine prograde *P–T* path of the two micaschist samples (GM1 and GM13). In order to consider progressive garnet fractionation, three pseudosections have been calculated for each sample in the *P–T* range 2–10 kbar and 450–700°C. The three pseudosections were used to model (i) garnet core growth (measured bulk composition), (ii) garnet mantle growth (subtracting the composition of garnet core from the measured bulk composition), and (iii) garnet rim growth (subtracting the composition of garnet core + mantle from the measured bulk composition) (see details about garnet fractionation in Appendix S6). In both samples, garnet fractionation results in the displacement to higher *T* of the garnet-in line and in the enlargement of the staurolite stability field.

6.1.1 | Garnet-staurolite micaschist (GM1)

In sample GM1, garnet is stable above ~500°C and its modal amount increases towards higher *P* and *T* conditions (Figure 9a). Comparison of the measured garnet core composition (spss = 15 mol.%, alm = 57 mol.%, py = 4 mol.% and grs = 21 mol.%) and the corresponding garnet isopleths suggests that garnet core crystallized at 4–6 kbar and 510–530°C. This *P–T* range comprises several narrow fields with the main association g-mu-chl-ilm-q and the presence or absence of minor biotite, magnetite, plagioclase, and calcic amphibole.

Considering an average composition of the garnet mantle domains (spss = 5 mol.%, alm = 70 mol.%, py = 5 mol.% and grs = 17 mol.%), the calculated isopleths suggest that garnet mantles equilibrated in the field g-bi-chl-mu-ilm-mt-q ± hb at 540–550°C and 5–7 kbar (Figure 9b). Garnet rims (alm = 82 mol.%, spss = 1 mol.%, grs = 3 mol.% and py = 12 mol.%) equilibrated in the *P–T* range 6–8 kbar and 640–660°C, in the g-pl-st-bi-mu-ilm-q ± ky stability fields (Figure 9c). Staurolite and kyanite mode isopleths suggest that a limited amount of staurolite (7–9 vol.%) and kyanite (~1 vol.%) developed at these *P–T* conditions. The thermodynamic modelling suggests that garnet rims equilibrated in a melt-absent field, just below the wet solidus (calculated at 650–660°C between 6 and 8 kbar).

6.1.2 | Garnet micaschist (GM13)

In sample GM13, the composition of $garnet_1$ cores (spss = 32 mol.%, alm = 51 mol.%, py = 3 mol.%, grs = 12 mol.%) implies that it equilibrated either in the field g-bi-chl-pl-mu-ilm-q or in the nearby g-bi-chl-pl-mu-ilm-q-mt field, at 4–5 kbar and 490–510°C (Figure 10a). Garnet-ilmenite thermometry (calibration of Pownceby et al., 1991) for ilmenite included in garnet cores indicates a *T* of 488 ± 36°C (Table S5), in agreement with thermodynamic modelling. From the average composition of $garnet_1$ mantle (spss = 15 mol.%, alm = 65 mol.%, py = 3 mol.% and grs = 14 mol.%), the calculated isopleths indicate that $garnet_1$ mantle equilibrated in the field g-bi-chl-pl-mu-ilm-q at 510–550°C and 4–6 kbar (Figure 10b). $Garnet_1$ rim composition (spss = 1 mol.%, alm = 79 mol.%, py = 15 mol.%, grs = 2 mol.%) indicates that it equilibrated in the field g-st-bi-pl-mu-ilm-q-mt, at 640–660°C and 6–7 kbar (Figure 10c). Staurolite mode isopleths suggest that only a limited amount of staurolite (~1 vol.%) developed in this field. The calculated solidus occurs at ~660°C between 3.5 and 10 kbar, suggesting that $garnet_1$ rim equilibrated in the absence of melt.

6.2 | Texture, composition and geochronology of zircon and monazite

6.2.1 | Muret orthogneiss (OG27)

Zircon crystals are prismatic in shape and 150 to 200 μm in length. Cathodoluminescence (CL) images reveal that zircon crystals either display a weak oscillatory zoning or are not zoned with grey CL emission. Most of them show a thin rim (maximum width of ~10 μm) characterized by bright CL emission (Figure 11a). Due to their small size, these thin rims have not been analysed. Zircon crystals commonly display inherited cores (50 to 100 μm in size) characterized by variable shape and zoning patterns (Figure 11a). Inherited cores show U and Th concentrations in the range 200–1,400 ppm and 33–280 ppm respectively, with Th/U ratios between 0.11 and 0.35 (Figure 11b). They yield concordant dates in the range 530–580 Ma and a single older date of 676 ± 17 Ma (2σ error). U-Pb analyses from zircon yield $^{206}Pb/^{238}U$ dates ranging from 446 ± 12 Ma to 407 ± 8 Ma (2σ error). Most analyses (34 out of 51) define a concordia age of 442.2 ± 2.0 Ma (95% c.i., MSWD (concordance + equivalence) = 1.4; *n* = 34; Figure 11c). Zircon displays

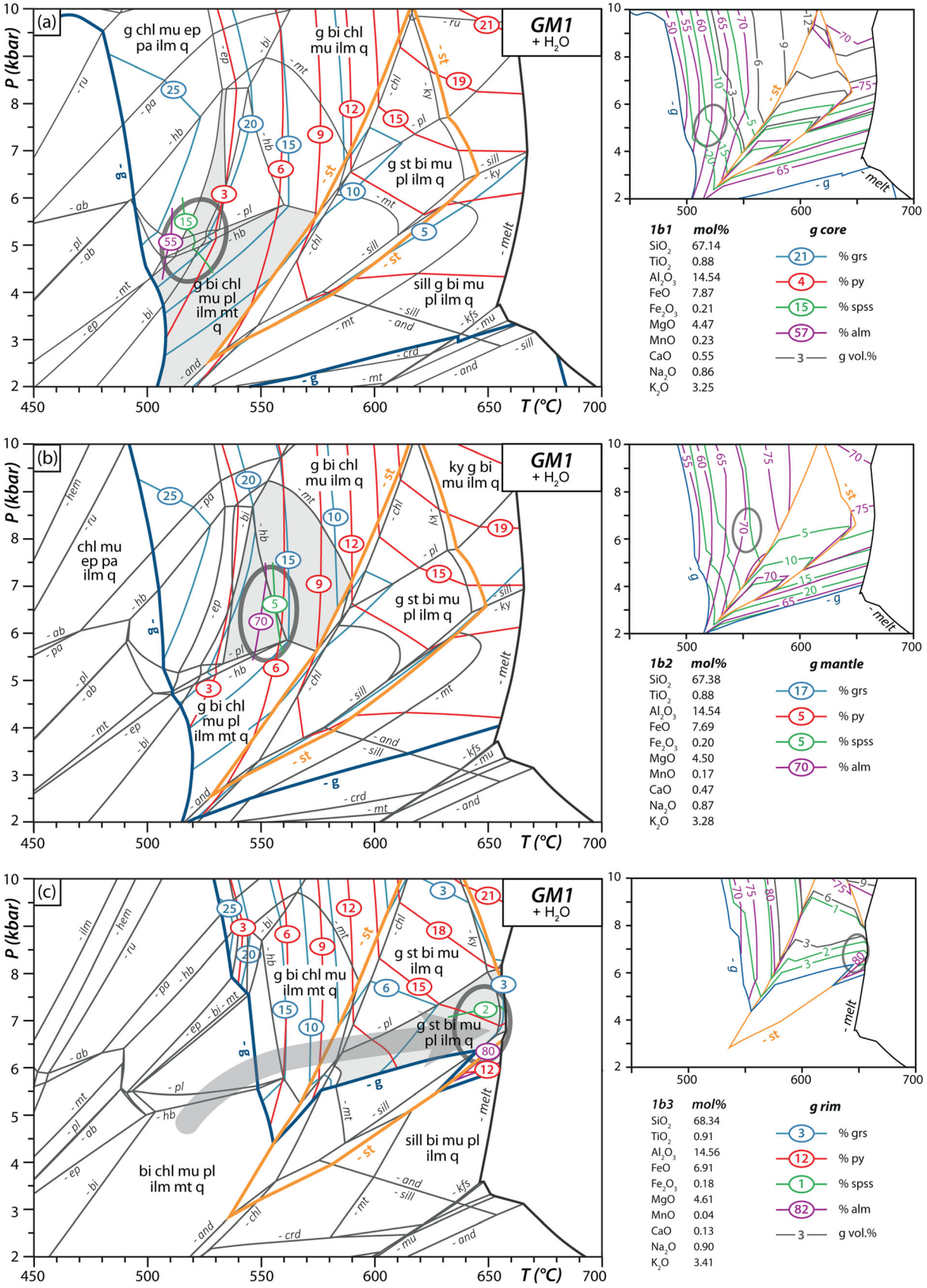

FIGURE 9 Legend on next page.

variable U (147–1,361 ppm) and Th (13–615 ppm) concentrations. Their Th/U ratios range between 0.01 and 0.54 (Figure 11b), with most of the zircon having Th/U ratios smaller than 0.2. Ti concentrations are in the range 4–15 ppm and 5–13 ppm for inherited cores and magmatic crystals, respectively (Table S10). Chondrite-normalized REE patterns are similar for the inherited cores and magmatic crystals, with HREE enrichment, steep HREE patterns ($Dy_N/Yb_N = 0.10–0.21$), a Ce anomaly, and negative Eu anomaly ($Eu/Eu_* = 0.018–0.067$; Figure 11d).

6.2.2 | Garnet-staurolite micaschist (GM1)

Zircon crystals are euhedral to rounded and up to 100 μm in length. Most crystals display a bright core and a dark rim (Figure 12a). Cores have variable size (from 10 to 80 μm in length) and shape (from rounded to poorly elongated), and some are partially resorbed. Most of them are characterized by oscillatory zoning. Rims are up to 40 μm thick and usually display low CL emission. A few crystals (6 out of 59 investigated), that are roughly 60 μm in length, do not show distinct core and rim domains. They are homogeneous or have weak patchy zonation with low CL emission (Figure 12a). Cores display variable U (163–1,400 ppm) and Th (20–960 ppm) contents, and their Th/U ratio ranges from 0.02 to 0.69 (Figure 12b). U and Th concentrations in the rims and homogeneous crystals are in the range 800–3,250 ppm and 3–23 ppm, respectively, with very low Th/U ratios (0.001–0.012; Figure 12b). Ti concentrations in zircon rims and homogeneous crystals are in the range 1–6 ppm. Zircon rims and homogeneous crystals exhibit HREE patterns with moderate positive slopes ($Dy_N/Yb_N = 0.11–0.90$) weak Ce anomalies and weak negative Eu anomalies ($Eu/Eu_* = 0.20–0.41$). Two analyses display an almost flat pattern from Dy to Tm, followed by an increase in Yb and Lu (Figure 12d). Trace element composition of detrital cores has not been analysed.

Owing to their small size, only 17 zircon cores were successfully analysed (i.e. analyses avoided mixing with rims). They yield concordant dates ranging from ~1800 to ~590 Ma (Figure 12b), with a cluster of 11 dates between 590 and 735 Ma, 2 around 810–820 Ma, 3 between 950 and 1,070 Ma, and an older date at 1777 ± 29 Ma. Zircon rims and homogeneous crystals yield dates in the range 315–290 Ma and define a concordia age of 304.0 ± 1.7 Ma (95% c.l.; MSWD = 0.8; $n = 25$; Figure 12c).

Monazite occurs most commonly in garnet rims (zone C, Figure S1b) but is also observed as rare crystals in garnet mantles (zone B, Figure 13a) and in minor amounts in the matrix. No monazite is observed in garnet cores (zone A). Monazite included in garnet has mostly prismatic shape with length ranging from 30 to 200 μm and is oriented parallel to the internal foliation defined by quartz inclusions in zone B (Figure 13a). Sharp grain boundaries with the host garnet are observed (Figure 13b). Monazite in the matrix has variable size (20 to 100 μm), anhedral crystal shapes, resorbed grain boundaries, and is locally replaced by allanite. Monazite crystals in both garnet and matrix contain quartz inclusions and are internally homogeneous in BSE imaging (Figure 13b). U-Th-Pb dating was performed primarily on monazite included in garnet because of its meaningful textural position and better state of preservation.

The two types of monazites yield dates and trace element composition indistinguishable within error. $^{206}Pb/^{238}U$ dates range from 295 ± 29 and 356 ± 36 Ma and define a Concordia age for the system $^{206}Pb/^{238}U$ versus $^{207}Pb/^{235}U$ of 324.0 ± 6.0 Ma (95% c.i.; $MSWD_{(concordance + equivalence)} = 0.5$; $n = 18$; Figure 13c). $^{208}Pb/^{232}Th$ dates range from 291 ± 27 and 433 ± 30 Ma and define a Concordia age for the system $^{206}Pb/^{238}U$ versus $^{208}Pb/^{232}Th$ of 319.6 ± 4.0 Ma (95% c.i.; $MSWD_{(concordance + equivalence)} = 0.8$; $n = 24$; Figure S3a).

The Y content of monazite is generally lower than 2,200 ppm, the Th content is between 5.0 and 7.5 wt.%, with Th/U ratios of 10–21, and the Sr content is between 550 and 1,250 ppm (Table S13). Chondrite-normalized patterns show a very weak to absent negative Eu anomaly ($Eu/Eu_* = 0.97–1.00$) and the typical depletion in HREE in monazite (Figure 13d).

FIGURE 9 Pressure–temperature (*P*–*T*) pseudosections calculated for the garnet-staurolite micaschist GM1, considering progressive garnet fractionation. Some fields are not labelled for the sake of clarity; their assemblages can be deduced from assemblages in adjacent fields. The garnet-in, staurolite-in, and melt-in lines (wet solidus) are highlighted with thick blue, orange, and black lines, respectively. Grey circles indicate the *P*–*T* conditions at the three stages of garnet growth. (a) Pseudosection calculated for the bulk composition 1b1 (obtained by XRF) and used for constraining the *P*–*T* conditions of equilibration of garnet core. Garnet isomodes are shown in the small plot on the right-hand side. (b) Pseudosection calculated for the bulk composition 1b2 (after garnet core fractionation) and used for constraining the *P*–*T* conditions of equilibration of garnet mantle. (c) Pseudosection calculated for the bulk composition 1b3 (after garnet core and mantle fractionation) and used for constraining the *P*–*T* conditions of equilibration of garnet rim. The grey arrow indicates the *P*–*T* evolution as inferred from the three pseudosections [Colour figure can be viewed at wileyonlinelibrary.com]

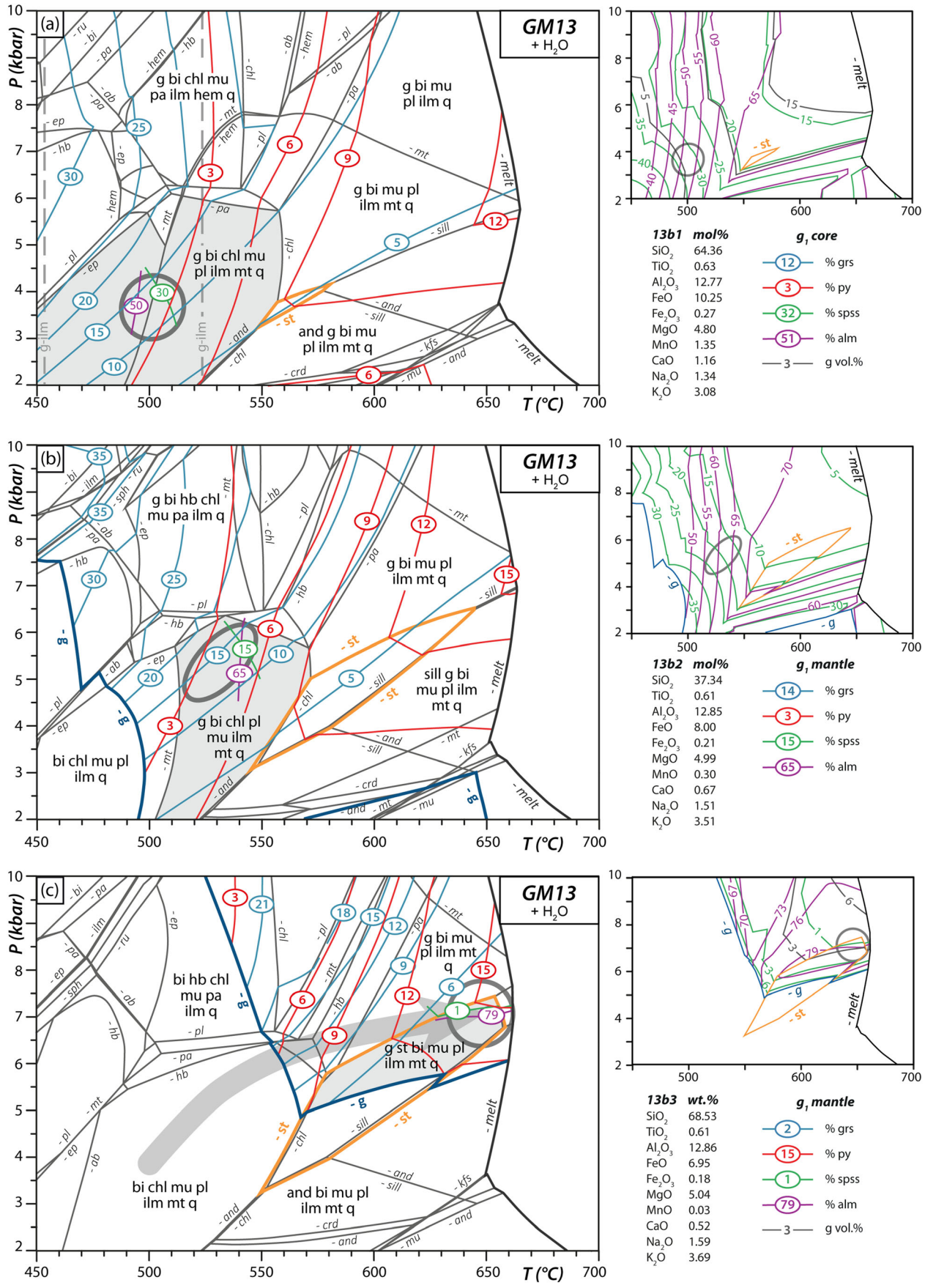

FIGURE 10 Legend on next page.

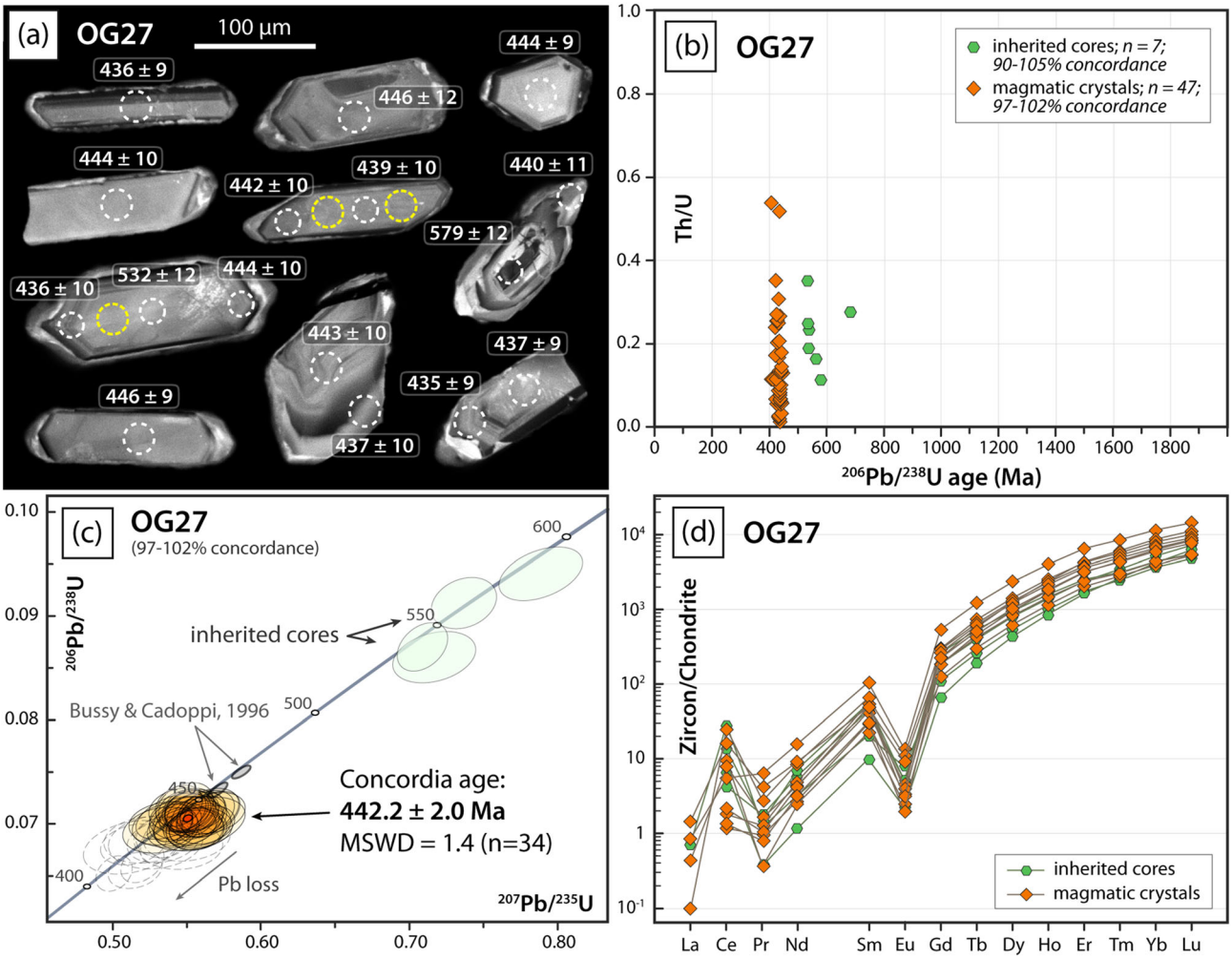

FIGURE 11 (a) Cathodoluminescence images of zircon from orthogneiss sample OG27. Dashed white and yellow circles represent the location of the LA-ICP-MS U-Pb (given as $^{206}Pb/^{238}U$ ages) and trace elements analyses, respectively. (b) Th/U ratio versus age plot for sample OG27. (c) Concordia diagram for zircon from sample OG27. Green ellipses indicate dates from inherited cores, whereas yellow ellipses indicate dates from magmatic crystals. Empty dashed ellipses represent dates excluded from magmatic Concordia age calculation. (d) Zircon trace element composition for sample OG27. REE patterns are normalized to chondrite values (McDonough & Sun, 1995) [Colour figure can be viewed at wileyonlinelibrary.com]

6.2.3 | Garnet micaschist (GM13)

Zircon crystals are up to 100 µm in length, rounded to prismatic in shape, and display clear cores and rims. Cores are prismatic and exhibit high CL emission with mostly oscillatory zoning patterns (Figure 12e). Rims are less than 10 µm thick with CL emission ranging from dark (in the inner part) to bright (in the outer part). Due

FIGURE 10 Pressure–temperature (*P*–*T*) pseudosections calculated for the garnet micaschist GM13, considering progressive garnet fractionation. Some fields are not labelled for the sake of clarity; their assemblages can be deduced from assemblages in adjacent fields. The garnet-in, staurolite-in, and melt-in lines (wet solidus) are highlighted with thick blue, orange, and black lines, respectively. Garnet composition is used to constrain the *P*–*T* conditions (indicated by a grey circle) at the three stages of garnet growth.
(a) Pseudosection calculated for the local bulk composition 13b1 (obtained by area scan method) and used for constraining the *P*–*T* conditions of equilibration of $garnet_1$ core. Garnet isomodes are shown in the small plot on the right-hand side. (b) Pseudosection calculated for the bulk composition 13b2 (after $garnet_1$ core fractionation) and used for constraining the *P*–*T* conditions of equilibration of $garnet_1$ mantle. (c) Pseudosection calculated for the bulk composition 13b3 (after $garnet_1$ core and mantle fractionation) and used for constraining the *P*–*T* conditions of equilibration of $garnet_1$ rim. The grey arrow indicates the *P*–*T* evolution as inferred from the three pseudosections [Colour figure can be viewed at wileyonlinelibrary.com]

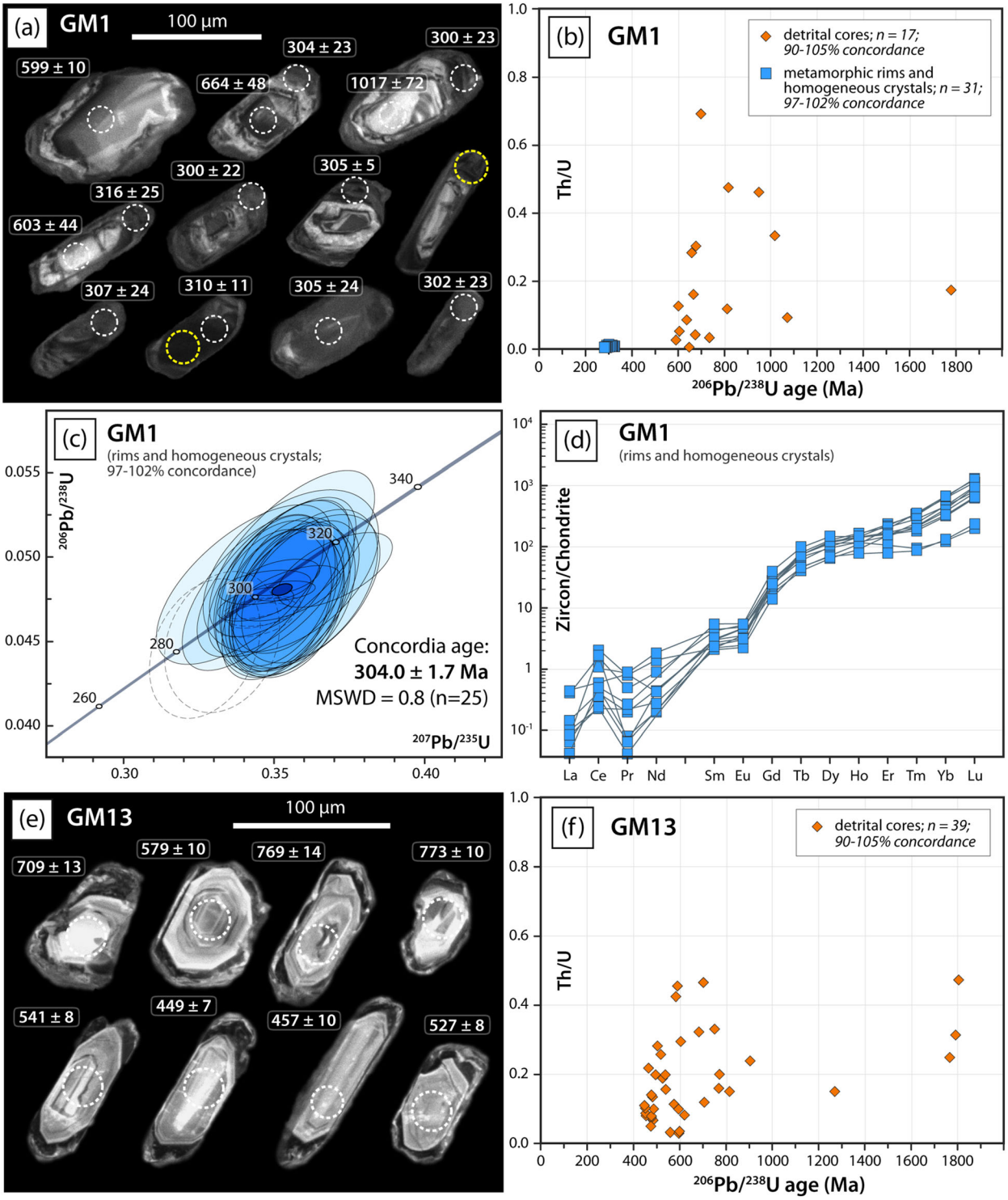

FIGURE 12 (a) Cathodoluminescence images of zircon from garnet-staurolite sample GM1. Dashed white and yellow circles represent the location of the LA-ICP-MS U-Pb (given as $^{206}Pb/^{238}U$ ages) and trace elements analyses, respectively. Zircons in the first and second row display core and rim domains, whereas zircons in the bottom row are internally homogeneous. (b) Th/U ratio versus age plot for sample GM1. (c) Concordia diagram for zircon dates (metamorphic rims and crystals) for sample GM1. Empty dashed ellipses represent data excluded from Concordia age calculation. (d) Trace element compositions of metamorphic zircon rims and homogeneous crystals for garnet-staurolite sample GM1. REE patterns are normalized to chondrite values (McDonough & Sun, 1995). (e) Cathodoluminescence images of zircon from garnet micaschist sample GM13. Dashed white circles represent the location of the LA-ICP-MS U-Pb analyses (given as $^{206}Pb/^{238}U$ ages). (f) Th/U ratio versus age plot for zircon from garnet micaschist sample GM13 [Colour figure can be viewed at wileyonlinelibrary.com]

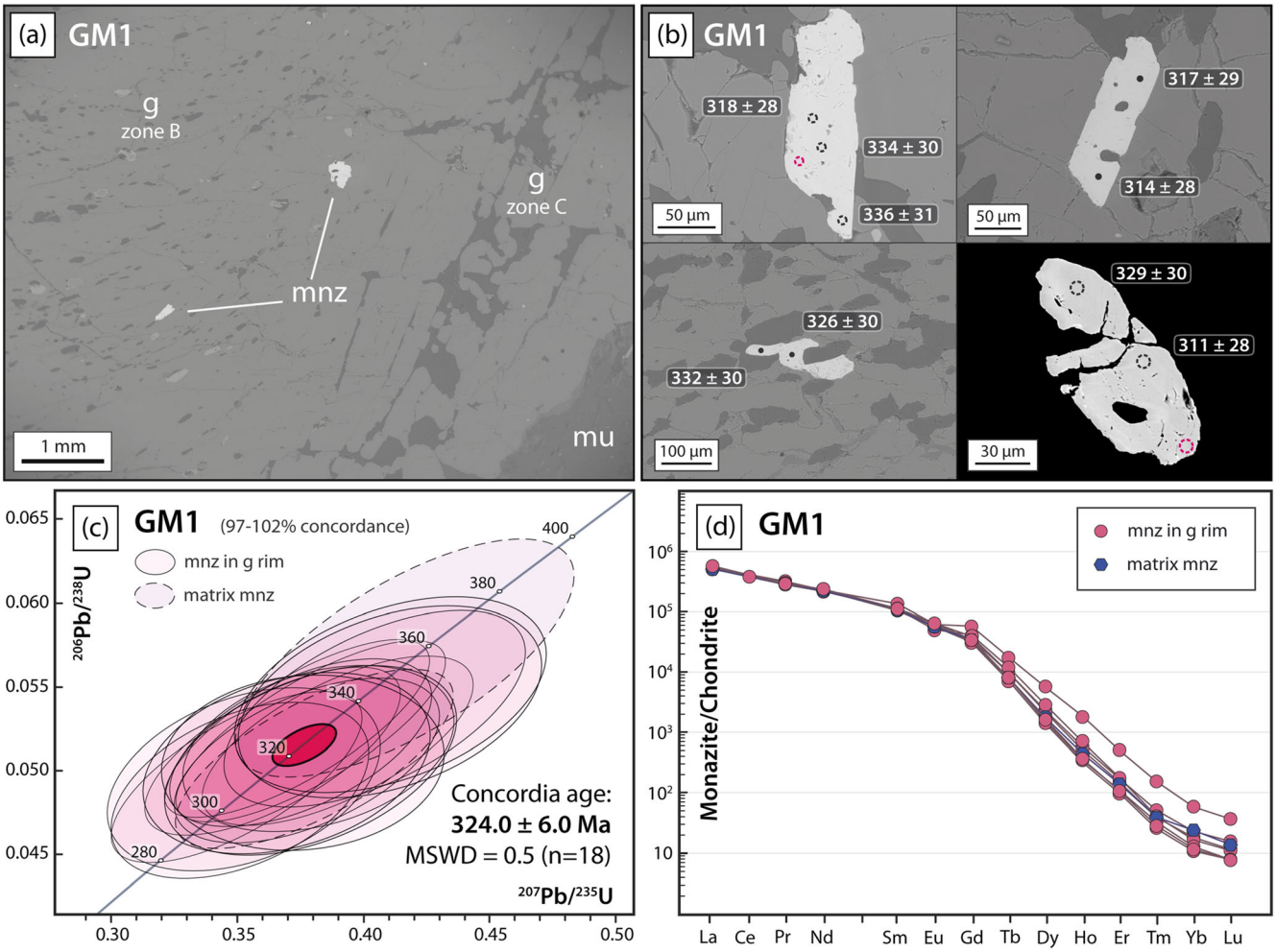

FIGURE 13 (a) Backscattered electron image (BSE) of monazite included in garnet mantles and rims (zone B and C), for sample GM1. Monazite is oriented parallel to the internal foliation in garnet. (b) BSE images of monazite. Analytical spots are indicated by black dashed circles or dots (8 µm diameter) for isotopic dating (dates given as $^{208}Pb/^{232}Th$), and by pink dashed circles for trace element analyses. (c) Concordia diagram for monazite from garnet-staurolite micaschist sample GM1. (d) Monazite trace element composition for sample GM1. REE patterns are normalized to chondrite values (McDonough & Sun, 1995) [Colour figure can be viewed at wileyonlinelibrary.com]

to their small size, rims have not been analysed. U and Th concentrations in the core range from 50 to 2000 ppm and from 15 to 300 ppm respectively, with Th/U ratios varying from 0.03 to 0.47 (Figure 12f). The 37 zircon cores yield concordant dates scattered between ~450 and ~1800 Ma (Figure 12f). The most abundant zircon population (27) is between ~450 and ~620 Ma, and the youngest single date is 449 ± 7 Ma. Older zircons populations are between ~700 and ~900 Ma (eight dates) and at ~1800 Ma (two dates).

7 | DISCUSSION

The Punta Muret area exposes a kilometre-scale pre-Alpine low-strain volume that escaped pervasive Alpine deformation and high-pressure metamorphism and represents an excellent case study for reconstructing the Palaeozoic evolution of the Dora-Maira Massif. The low-strain volume comprises a kilometre-scale lenticular orthogneiss body (the Muret orthogneiss) and garnet-staurolite micaschist. Both lithologies preserve a pre-Alpine amphibolite-facies foliation oriented at high angle with respect to the dominant high-pressure Alpine fabric observed outside the low-strain volume. A detailed structural analysis of this domain is out of scope of this paper, which is devoted to the petrological record of pre-Alpine history.

7.1 | Nature and timing of pre-Alpine magmatism

The Muret orthogneiss is a peraluminous granodioritic body and partially preserves relicts of its igneous

mineralogy (such as the alkali feldspar porphyroclasts) and microgranular enclaves. Field observations along the north-western contact between the Muret orthogneiss and the garnet-staurolite micaschist show that (i) there is no evidence for an increasing strain, (ii) tourmaline-quartz veins occurs in the garnet-staurolite micaschist, and (iii) the proportion of alkali feldspar porphyroclasts in the Muret orthogneiss decreases towards the contact. These observations may be interpreted as recording a chilled pluton margin and suggest that the protolith of the Muret orthogneiss (likely a granodioritic body) intruded the meta-sedimentary country rocks. Subsequently, both lithologies were involved in an amphibolite-facies deformation, during which (i) the granodiorite was transformed into an orthogneiss, (ii) the contact with the country rocks was reoriented parallel to the main foliation in the orthogneiss, and (iii) the tourmaline-quartz veins were deformed and reoriented parallel to the pre-Alpine metamorphic foliation.

Zircon crystals from the Muret orthogneiss display features (shape, internal texture, and REE pattern) typical of magmatic zircon (Corfu et al., 2003; Hoskin & Schaltegger, 2003). Their HREE-enriched REE pattern and negative Eu anomaly are consistent with the crystallization of zircon from an evolved melt that had already crystallized plagioclase (Hoskin & Schaltegger, 2003). The low Th/U ratios (<0.2) shown by the majority of the zircon grains have been described in zircon from other peraluminous granitoids and interpreted as a diagnostic feature of peraluminous granitic magmatism (Lopez-Sanchez et al., 2016). This is in a good agreement with the whole rock major element signatures. Inherited cores, characterized by variable size, shape, and internal texture, have been observed in several zircon crystals from the Muret orthogneiss. Their REE patterns are typical of magmatic zircon, with HREE enrichment and negative Eu anomaly (Figure 11d; Hoskin & Schaltegger, 2003) and yield concordant dates at c. 530 and c. 580 Ma. The relatively high zircon inheritance and the peraluminous character of the Muret orthogneiss may suggest that it crystallizes from S-type granitic melts at $T < 800^{\circ}C$ characterized by moderate water contents (Bea et al., 2021; Chappell & White, 2001; Miller et al., 2003).

The U/Pb early Silurian date of 442 ± 2 Ma obtained in this study is considered as the crystallization age of the granodioritic magma. This age is slightly younger with respect to a previous estimate at 457 ± 2 Ma for the Muret orthogneiss, obtained by Bussy and Cadoppi (1996) using isotope dilution thermal ionization mass spectrometry (ID-TIMS). This difference may be related to the unavoidable mixing between inherited cores and magmatic crystals with the isotope dilution method.

7.2 | Timing of pre-Alpine sedimentation

The timing of the pre-Alpine sedimentation of the protolith of the micaschists may be constrained combining field and isotopic data. Due to the small size of the zircon grains and the partial resorption of their detrital cores, a limited and nonstatistically significant number of grains (Andersen, 2005; Malusà et al., 2013; Vermeesch, 2004) were analysed in the micaschists (samples GM1 and GM13). Therefore, a cautious and rather speculative maximum deposition age of the sediments now constituting the micaschists may be suggested (Fedo et al., 2003; Vermeesch, 2004).

In the garnet-staurolite micaschist (sample GM1, low-strain volume), the youngest cluster defined by at least three concordant analyses (Dickinson & Gehrels, 2009) yields a weighted average date of 598 ± 9 Ma (MSWD = 0.12), which corresponds to an Ediacaran age. Field data suggest that the protolith of the Muret orthogneiss may have intruded the sediments now constituting the garnet-staurolite micaschists. Given the well-established age of the granitic protolith in the earliest Silurian (442 ± 2 Ma), the pre-Alpine sedimentation should be older than c. 440 Ma. Therefore, the sediments now forming the garnet-staurolite micaschist were deposited during the Ediacaran to Ordovician time.

In the garnet micaschist (sample GM13, outside the low-strain volume), the youngest cluster of concordant data yields a U/Pb date of 453 ± 4 Ma (weighted average; MSWD = 0.72, $n = 4$), that is, a younger maximum age of deposition (Upper Ordovician) for the sedimentation than for sample GM1 (garnet-staurolite micaschist).

7.3 | *P–T* conditions of the pre-Alpine metamorphism

The low-strain volume of the Muret Unit preserves evidence of pre-Alpine metamorphism and deformation. In the orthogneiss, Ti-rich biotite and low-Si muscovite define the main pre-Alpine foliation, whereas pre-Alpine garnet is found dispersed in the matrix. Metapelitic country rock displays pre-Alpine garnet (and its inclusions) and a pre-Alpine foliation marked by low-Si muscovite and staurolite (now pseudomorphed). The pre-Alpine foliation in the orthogneiss and in the garnet-staurolite micaschist displays the same orientation. Outside the undeformed domain, the garnet micaschist cropping out on the crest of the Punta Muret is dominated by an Alpine high-pressure foliation, discordant to the pre-Alpine foliation observed in the low-strain volume. In this high-strain volume, the first generation of garnet

(and its inclusions, namely quartz, ilmenite, muscovite and graphite) is the only record of pre-Alpine metamorphism. $Garnet_1$ is overgrown by a second generation of garnet during the Alpine cycle.

Thermodynamic modelling based on garnet chemical composition was used to constrain the pre-Alpine, prograde *P–T* evolution of the northern Dora-Maira Massif. In the garnet-staurolite micaschist and garnet micaschist, pre-Alpine garnet grew following similar *P–T* trajectories, from 4 to 5 kbar ~500°C to 6–7 kbar ~650°C. The distribution and orientation of garnet isomodes (Figures 9a,c and 10a,c) suggest that most garnet growth occurred during early prograde history.

The observed changes in Y, Zr, HREE, and P content in garnet may be explained by changes in the stability fields of major and accessory phases. Zircon, xenotime, and Y-rich epidote/allanite are all REE-bearing minerals that potentially can represent sinks for Y + REE. Allanite and Y-rich epidote appear as unlikely sources because, in this case, LREE peaks in garnet would be also expected, whereas they are not observed. Zircon and xenotime are both enriched in HREE with respect to LREE and may display a negative Eu anomaly. Because xenotime has not been observed in garnet, whereas numerous tiny and partially dissolving zircon crystals are found in garnet cores and mantles (zones A and B), we suggest that zircon was partially dissolved during garnet growth, providing a source of Y + HREE. The increase of P at garnet rims (zone C) and the occurrence of monazite in garnet mantles (zone B) and rims (zone C) may result from the breakdown of apatite, which is observed only in garnet core (zone A). This reaction may also explain the slight increase in MREE at the transition between the garnet mantle-garnet rim as reported in other studies (e.g. Manzotti, Bosse, et al., 2018; Regis et al., 2014).

Element diffusion in garnet becomes an efficient mechanism above ~600°C (Caddick et al., 2010; Ganguly, 2010; Yardley, 1977). We assume that diffusive relaxation did not significantly modify garnet growth zoning in the studied samples, because (i) *T* never exceeded 650°C and (ii) garnet porphyroblasts are moderately large (4 to 10 mm in size) (Caddick et al., 2010). In both the modelled micaschists, garnet isopleths indicate that garnet rim was stable with staurolite at peak *P–T* conditions. Staurolite (now pseudomorphed) has been only observed in sample GM1, as part of the low-strain domain, as inclusion in the garnet rims and marking a pre-Alpine foliation. By contrast, staurolite (or pseudomorphs after staurolite) has not been identified in sample GM13. Calculated staurolite mode isopleths for sample GM13 indicate the formation of a very limited amount of staurolite (~1 vol.%) for the estimated *P–T* conditions, possibly explaining why staurolite pseudomorphs have not been found in this rock. The lower Al_2O_3 content of sample GM13 with respect to sample GM1 (Figure S4) may have also prevented the formation of a large amount of staurolite. Lastly, sample GM13 has been collected along the crest of the Punta Muret, outside the low-strain domain. Therefore, we cannot exclude that the pervasive Alpine metamorphism and deformation may have completely obliterated staurolite and its pseudomorphs within this metapelite. Thermodynamic modelling for the micaschist sample GM1 indicates that less than 5 vol.% of biotite is stable during the prograde evolution (i.e. during the growth of garnet cores and mantles), whereas ~20 vol.% of biotite is stable at peak *P–T* conditions (i.e. during the growth of garnet rims) (Figure S5a,b,c). By contrast, ~20 vol.% of biotite is predicted to be stable in the micaschist sample GM13 during garnet growth (Figure S5d,e,f).

Field and petrographic observations and thermodynamic modelling indicate that the metapelites of the Muret Unit did not experience partial melting. Their pre-Alpine metamorphic evolution is typical of prograde Barrovian metamorphism from the garnet zone to the staurolite zone (e.g. Gaidies et al., 2015). Our observations in the Muret Unit are therefore consistent with previous observations by Cadoppi (1990) in the same unit. We have not been able to confirm the presence of garnet-biotite-sillimanite assemblages in the Muret Unit, attributed to the granulite facies, as postulated by Bouffette et al. (1993).

7.4 | Timing of the pre-Alpine metamorphism

Direct evidence for the age of the pre-Alpine metamorphism may be gathered from the study of monazite and zircon from the garnet-staurolite micaschist (sample GM1). Monazite is found in the external part of garnet (zones B and C) and in the matrix, whereas zircon is present as minute grains in garnet cores and mantles (zones A and B) and as larger grains in the matrix. Interpreting the dates of monazite and zircon rely on a combination of textural, chemical and isotopic data.

Monazite included in garnet mantles and rims (zones B and C) yields a single age cluster at 324 ± 6 Ma. Monazite displays sharp grain boundaries with enclosing garnet and ovoid or prismatic shapes, suggesting textural equilibrium with garnet. No evidence for chemical zoning in monazite has been found. Calculated REE partition coefficients between monazite and enclosing garnet show a negative trend, similar to those previously reported for metapelitic rocks where monazite and garnet grew in equilibrium at 500–600°C (Hacker et al., 2019,

Figure S3b). These temperature estimates are consistent with those derived from the thermodynamic modelling on garnet growth in our sample. Therefore, we conclude that monazite and garnet rims crystallized near peak *P* conditions (~6 kbar), and we consider the age of 324 ± 6 Ma as a robust estimate of the age of the pre-Alpine metamorphism in the Dora-Maira Massif.

Zircon grains are much more heterogenous than monazite crystals in terms of texture, composition and age. Apart from detrital cores, which constitute the largest fractions of the analysed zircons, only a few crystals display rim domains or are homogeneous (without detrital cores). No differences in geochemistry and U-Pb dates have been observed between zircon rims and homogeneous crystals: Both show very low Th/U ratios (0.001–0.006) and low REE concentrations, typical features found in metamorphic zircon (e.g. Corfu et al., 2003; Rubatto, 2017). These zircons yield a date of 304 ± 2 Ma (Figure 12c), which is 20 Ma younger than the monazite metamorphic age, and needs careful consideration before interpretation.

In a rock containing detrital grains, zircon dissolution occurs during prograde metamorphism whereas zircon should grow mainly during late stage of exhumation and cooling (e.g. Kelsey et al., 2008; Kelsey & Powell, 2011; Kohn et al., 2015) even under fluid-present greenschist-facies conditions (e.g. Hoiland et al., 2018). In our sample, there is evidence for monazite growth at peak *P–T* conditions in equilibrium with garnet rim. By contrast, the moderate positive slope of HREE patterns in metamorphic zircon from sample GM1 suggests that garnet and zircon did not grow in equilibrium (e.g. Rubatto, 2002). Therefore, zircon growth occurred after peak *P–T* conditions.

The weak negative Eu anomaly of the metamorphic zircon grains may suggest that during zircon growth, plagioclase was present but in a limited modal amount. This is consistent with the calculated modal isopleths, indicating a limited amount of plagioclase (up to 6 vol.%). A larger negative Eu anomaly would be expected if the rock underwent partial melting and crystallized feldspars, as observed in amphibolite-facies partially melted metasediments (e.g. Manzotti, Rubatto, et al., 2018). The weak Eu anomaly is consistent with field observations and thermodynamic modelling, suggesting that this rock never underwent partial melting.

It is therefore probable that the small amount of metamorphic zircon observed in sample GM1 may have grown during retrograde cooling. Several rock-forming minerals, such as rutile, ilmenite, amphibole, garnet, and magnetite may contain significant concentration of Zr (Bea et al., 2006), and their destabilization may induce zircon growth (Kohn et al., 2015). Rutile is not found in the studied rock during the pre-Alpine history and indeed its presence is not predicted by the thermodynamic model. Amphibole and magnetite are predicted to be stable in a narrow range between 450°C and 600°C, and the calculated modal isopleths indicate that their modal amount is very low (Figure S6). We therefore conclude that amphibole and magnetite do not play a major role in zircon consumption and growth in the studied sample. By contrast, during cooling and decompression garnet may have been partially consumed, providing a potential source of Zr. Garnet consumption (and zircon growth) may have been triggered by fluid infiltration during the early exhumation and cooling (Figure 14) at 304 ± 2 Ma. In addition, the calculated modal isopleths of ilmenite indicate that also ilmenite is consumed during early decompression (Figure S6), possibly providing an additional source of Zr, although its calculated modal amount is low.

8 | PRE-ALPINE EVOLUTION OF THE DORA-MAIRA MASSIF

Because the studied area is characterized by a kilometre-scale low-strain volume where the Alpine deformation is absent or very weak, it constitutes a reference section for unravelling the pre-Alpine evolution of the Dora-Maira Massif (Figures 14 and 15). This is summarized below, with a comparison with other Variscan basement units in and outside the Alpine belt.

8.1 | Palaeozoic sedimentation and magmatism

During the Early Palaeozoic, the Dora-Maira Massif, like the other Briançonnais-derived units, belonged to the northern Gondwana palaeomargin (Franke et al., 2020). There, Ediacaran to Ordovician siliciclastic sedimentation took place in a marine environment. This early Palaeozoic episode has been identified in many places throughout the Alpine basement, such as the Austroalpine nappes (Heinrichs et al., 2012; Mandl et al., 2018) and in the Adula nappe (Liati et al., 2009). Outside the Alpine belt, Early Palaeozoic sequences are also widespread, for example, in the Tuscan Appennine (Paoli et al., 2017; Pieruccioni et al., 2018), the Elba Island (Sireevag et al., 2016), or the pre-Sardic successions in Sardinia (Cocco et al., 2018).

A major episode of granitic to rhyolitic magmatism occurred throughout the northern Gondwana palaeomargin during the Ordovician. The protolith of the Muret orthogneiss may represent one of the latest

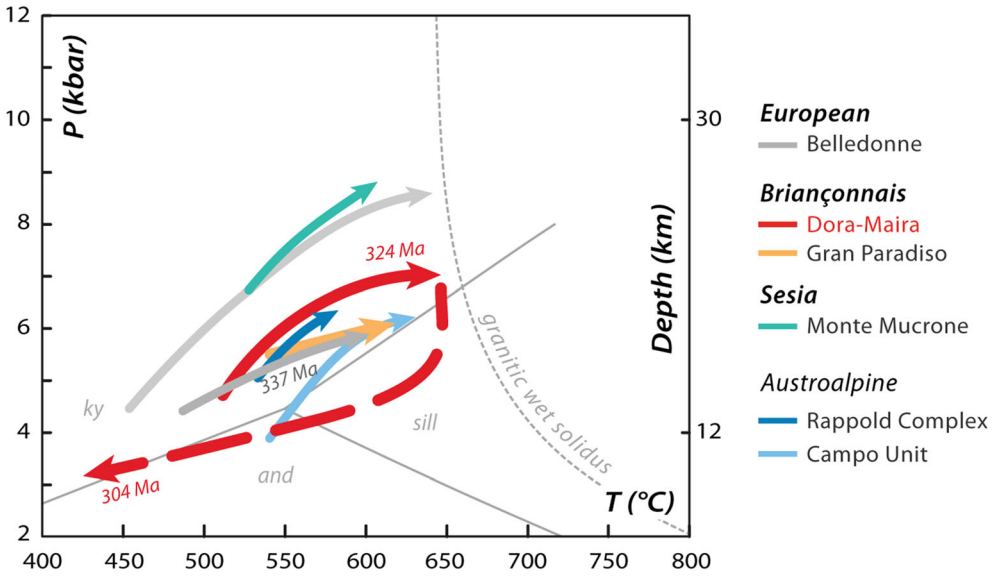

FIGURE 14 A compilation of the Barrovian *P–T–t* paths obtained for the Muret Unit in the Dora-Maira Massif (red arrow) and in other localities in the Alps. All pressure–temperature (*P–T*) paths have been obtained by modelling the garnet growth zoning. Literature data are from the following: Belledonne (Fréville et al., 2018); Gran Paradiso (Le Bayon et al., 2006); Sesia (Robyr et al., 2014); Rappold Complex (Gaidies et al., 2008); Campo Unit (Petri et al., 2016) [Colour figure can be viewed at wileyonlinelibrary.com]

manifestations of this episode, although its early Silurian age (c. 440 Ma) is slightly younger than the main episode recorded in nearby areas (c. 460 Ma) (Alvaro et al., 2020; Ballèvre et al., 2012; Pouclet et al., 2017). The Muret orthogneiss is the only Early Palaeozoic granitoid known so far in the Internal Crystalline Massifs. However, Ordovician magmatism is widespread in the Alps and has been dated in the External Massifs, in the Briançonnais basement, in the Sesia-Dent Blanche (Gilotti et al., 2016; Liermann et al., 2002), and in the Southalpine basement (for a review see Ballèvre et al., 2018; Bergomi et al., 2017).

Folded layers of marbles up to few decametres in thickness are found in the Muret Unit, outside the undeformed lens studied here, as well as in nearby areas where they are sometimes mined for talc (Cadoppi et al., 2016). Marbles also occur in other units of the Dora-Maira Massif, such as the *UHP* Brossasco-Isasca Unit (Castelli et al., 2007; Ferrando et al., 2017; Groppo et al., 2007). The marble layers in the Brossasco-Isasca Unit are intercalated inside polycyclic micaschists similar to those studied here and also contain relicts of high-temperature, pre-Alpine, and minerals (Castelli et al., 2007; Ferrando et al., 2017; Groppo et al., 2007). Consequently, they cannot be considered as Mesozoic sediments folded together with the Palaeozoic basement during the Alpine orogeny. No direct evidence for the age of the protolith of the marbles has been found. However, as a whole, in the Gondwanan sequences, carbonate sedimentation is only present during the early Cambrian (the "Archaeocyathan limestones") (e.g. Pillola et al., 1998) and becomes much more widespread during the Devonian and the early Carboniferous (e.g. Pondrelli et al., 2020), in response to the migration of the Gondwana plate to northern, more equatorial, palaeo-positions (Franke et al., 2020). As a working hypothesis, it is therefore assumed that the marbles from the Dora-Maira Massif may derive either from Early Cambrian or Devonian limestones. In itself, involvement of the marbles into the pre-orogenic history is a first-order argument in favour of a Variscan crustal thickening.

8.2 | Variscan (Carboniferous) orogeny

The Palaeozoic (most probably Ediacaran to Devonian) succession was involved in a major tectonic episode, recorded in the studied area by intense ductile deformation, associated with prograde metamorphism ranging up to 6 kbar, 650°C, dated by monazite at 324 ± 6 Ma. This episode therefore belongs to the Variscan Orogeny (Franke et al., 2020), during which crustal thickening took place with the associated Barrovian metamorphism. The Variscan metamorphic history of the pre-Alpine basement in the Western and Central Alps (see reviews in Ballèvre et al., 2018 and Bergomi et al., 2017) displays two major episodes:

1. Variscan *HP* relicts are known in the External Crystalline Massifs (Belledonne and Argentera), where *HP* metamorphism in eclogites and granulites is dated at 350–330 Ma (Jacob et al., 2021; Rubatto et al., 2010). *HP* metamorphism in metapelites and eclogites is dated at 350–300 and 390–355 Ma in the northern and middle Adula Nappe, respectively (Liati et al., 2009; Sandmann et al., 2014). In the Briançonnais basement of the Western Alps, rare eclogites have been found in Switzerland (Grand Saint Bernard nappe: Rahn, 1991; Sartori, 1990; Thélin et al., 1990) and Italy (Savona Massif: Messiga et al., 1992). In the latter case, LA-

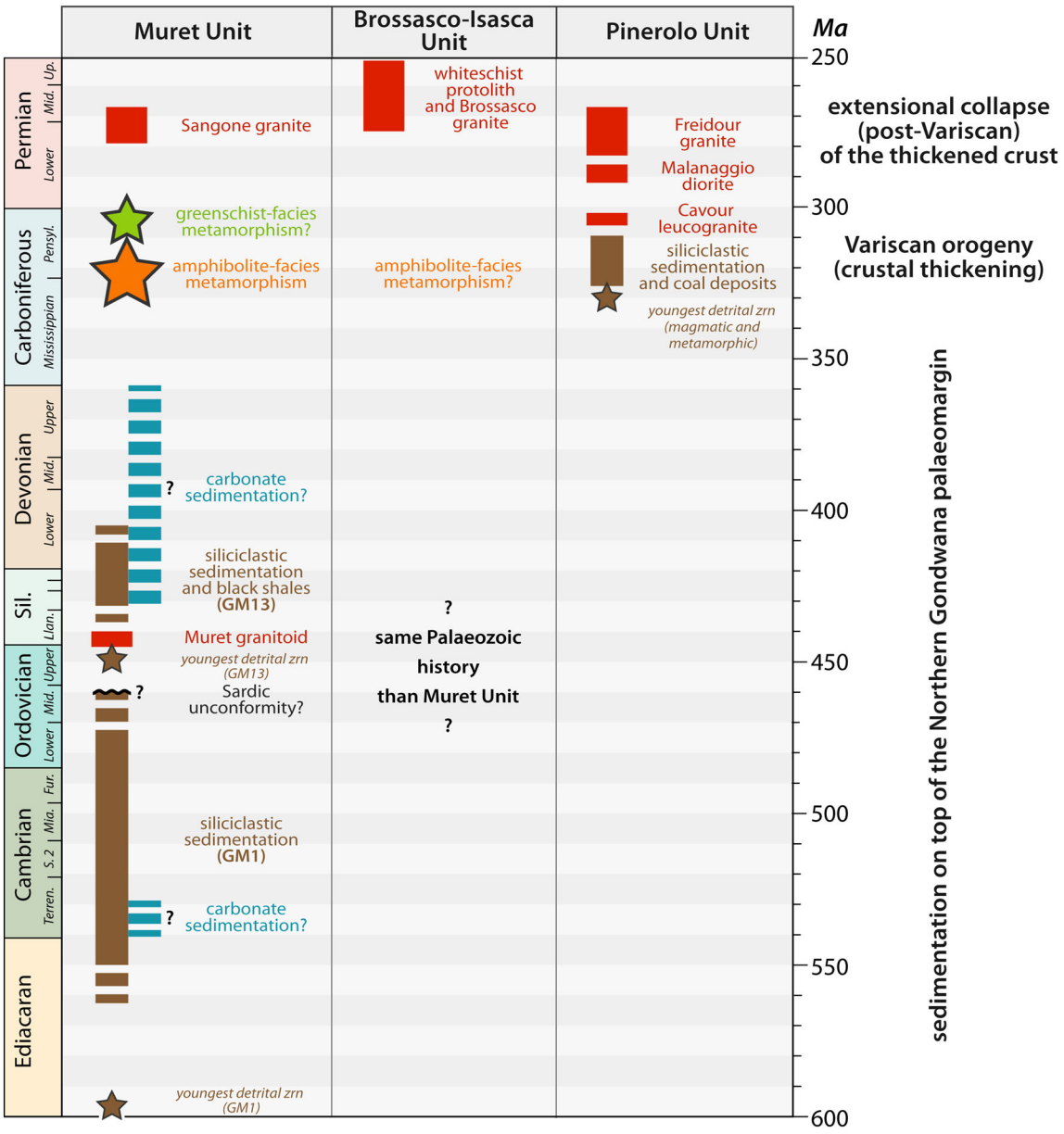

FIGURE 15 A summary of the pre-Alpine evolution of the Dora-Maira Massif. See text for further explanation [Colour figure can be viewed at wileyonlinelibrary.com]

ICP-MS U-Pb data on zircon from the eclogites are interpreted as recording the eclogite-facies metamorphism at 390–375 Ma (Giacomini et al., 2007). This *HP* episode is not recorded in the basement of the Dora-Maira Massif.

2. A Variscan Barrovian metamorphism (i.e. garnet-staurolite-biotite micaschist) is documented in the External Massifs of the Helvetic Domain (Belledonne: Fréville et al., 2018) and in the Briançonnais Domain (Sapey, Ruitor and Grand Saint Bernard: Burri, 1983; Bussy et al., 1996; Détraz & Loubat, 1984; Giorgis et al., 1999; Gouffon, 1993). Further east, it is documented in the Austroalpine Domain (Campo Unit: Petri et al., 2016; Rappold Complex: Gaidies et al., 2008). In these localities, the Alpine overprint is very weak or absent.

With increasing Alpine overprint, the pre-Alpine Barrovian metamorphism may become difficult to decipher. Evidence for such an episode may be found when (i) chloritoid aggregates after staurolite are identified and (ii) thermodynamic modelling based on garnet isopleths constrains prograde *P*–*T* paths at medium pressure (5–8 kbar) (Figure 14), like in the Gran Paradiso Massif (Le Bayon et al., 2006) and in the Sesia Zone (Robyr et al., 2014). In the southern Dora-Maira Massif, pre-

Alpine garnet and staurolite relicts have been found, but no attempt has been made to quantitatively describe their *P–T–t* evolution. The rocks from the Punta Muret, because they occur in a low-strain domain with respect to the Alpine deformation, offer the best example of pre-Alpine Barrovian metamorphism in the Dora-Maira Massif because (i) staurolite pseudomorphs can be identified using their prismatic shape and their replacement products (chloritoid) and (ii) garnet preserves its growth zoning (Figure 7a) and is amenable through thermodynamic modelling to constrain the pre-Alpine *P–T* path (Figure 9).

The timing of Variscan metamorphism of the Dora-Maira basement, here established at 324 ± 6 Ma, fits into the framework of the Barrovian metamorphism of the pre-Alpine basement. Likewise, in the Briançonnais (Ruitor Zone), the Barrovian metamorphism of the Mont Mort metapelites is dated at ~330 Ma (Bussy et al., 1996). Our ages from the Dora-Maira Massif are in agreement with preliminary data (microprobe analyses) obtained on monazite in the Monte Rosa Massif (Engi et al., 2001), although these ages were interpreted as recording the contact metamorphism of Carboniferous granites.

8.3 | Post-Variscan (Permian) history

During the Permian, numerous granitoid intrusions have taken place in the (future) Dora-Maira Massif (for a review, see Ballèvre et al., 2018 and Ballèvre et al., 2020). These intrusions are associated with contact metamorphism, whose relicts have been sparsely documented (Compagnoni & Rolfo, 2003). This indicates that (i) partial melting was proceeding in the lower crust during the Permian, allowing significant volumes of granitic melts to be produced in the lower crust, and (ii) the studied units were located in an upper crustal position, above the regions where partial melting was taking place. The thermal effect of this *HT*, Permian, episode, now largely identified in the Alpine belt (Kunz et al., 2018; Schuster & Stüwe, 2008) is not recorded in the polycyclic basement of the Dora-Maira Massif, to the difference of the Ivrea Zone and some units in the Sesia-Dent Blanche nappes.

9 | CONCLUSIONS

1. The Muret Unit in the northern Dora-Maira Massif is a slice of Palaeozoic basement that tectonically overthrust the Carboniferous meta-sediments of the Pinerolo Unit. The Muret Unit mainly comprises late Neoproterozoic to Ordovician meta-sediments intruded by a kilometre-scale early Silurian (442 ± 2 Ma, U-Pb LA-ICP-MS on zircon) granodioritic body (Muret orthogneiss).
2. Both the Muret orthogneiss and the meta-sedimentary countryrocks record amphibolite-facies conditions, characterized by garnet (preserving growth zoning) - staurolite parageneses. Thermodynamic modelling of garnet growth indicates a prograde *P–T* path from 4 to 5 kbar ~500°C to 6–7 kbar ~650°C. In the garnet-staurolite micaschist, U-Pb data from monazite allow the Barrovian metamorphism to be dated at 324 ± 6 Ma.
3. The characterization of the Variscan Barrovian metamorphism in the Dora-Maira Massif and the first robust age for the pre-Alpine metamorphism in the Internal Crystalline Massifs both confirm that the crustal rocks later involved in the Alpine subduction process did not belong to the lower crust but rather represent upper crustal slices.

ACKNOWLEDGEMENTS

This work was financially supported by the Swiss National Science Foundation (Advanced PostDoc Mobility: Project P300P2_147762, Ambizione: Project PZ00P2_161202) and a Starting Grant from Stockholm University to Paola Manzotti. Fieldwork from Francesco Nosenzo was partially supported by the Jubileumsdonationen K & A Wallenbergs Stiftelse 2020. Andreas Karlsson is thanked for assistance during SEM data acquisition. Victoria Pease is acknowledged for carefully reading and improving both the content and language of this paper. Many thanks are due to the two reviewers, Chiara Groppo and Stacy Phillips and to Clare Warren and Richard White for their editorial work. Informal reviews kindly provided by Christian Chopin and André Michard also helped improving the content of this paper.

DATA AVAILABILITY STATEMENT

The data that support the findings of this study are available in the supporting information of this article.

ORCID

Francesco Nosenzo https://orcid.org/0000-0003-1533-3011
Paola Manzotti https://orcid.org/0000-0002-6945-9878
Marc Poujol https://orcid.org/0000-0001-8682-2926
Michel Ballèvre https://orcid.org/0000-0001-6431-9051
Jessica Langlade https://orcid.org/0000-0002-2095-5272

REFERENCES

Alvaro, J. J., Sanchez-Garcia, T., Puddu, C., Casas, J. M., Diez-Montes, A., Liesa, M., & Oggiano, G. (2020). Comparative geochemical study on Furongian-earliest Ordovician (Toledanian) and Ordovician (Sardic) felsic magmatic events in South-

Western Europe: Underplating of hot mafic magmas linked to the opening of the Rheic Ocean. *Solid Earth*, *11*, 2377–2409. https://doi.org/10.5194/se-11-2377-2020

Andersen, T. (2005). Detrital zircons as tracers of sedimentary provenance: Limiting conditions from statistics and numerical simulation. *Chemical Geology*, *216*, 249–270. https://doi.org/10.1016/j.chemgeo.2004.11.013

Austrheim, H. (1987). Eclogitization of lower crustal granulites by fluid migration through shear zones. *Earth and Planetary Science Letters*, *81*, 221–232. https://doi.org/10.1016/0012-821X(87)90158-0

Austrheim, H. (2013). Fluid and deformation induced metamorphic processes around Moho beneath continent collision zones: Examples from the exposed root zone of the Caledonian mountain belt, W-Norway. *Tectonophysics*, *609*, 620–635. https://doi.org/10.1016/j.tecto.2013.08.030

Avigad, D., Chopin, C., & Le Bayon, R. (2003). Thrusting and extension in the southern Dora-Maira ultra-high-pressure massif (Western Alps): View from below the coesite-bearing unit. *The Journal of Geology*, *111*, 57–70. https://doi.org/10.1086/344664

Ballèvre, M., Camonin, A., Manzotti, P., & Poujol, M. (2020). A step towards unraveling the paleogeographic attribution of pre-Mesozoic basement complexes in the Western Alps based on U–Pb geochronology of Permian magmatism. *Swiss Journal of Geosciences*, *133*, 12.

Ballèvre, M., Fourcade, S., Capdevila, R., Peucat, J.-J., Cocherie, A., & Fanning, C. M. (2012). Geochronology and geochemistry of Ordovician felsic volcanism in the Southern Armorican Massif (Variscan belt, France): Implications for the breakup of Gondwana. *Gondwana Research*, *21*, 1019–1036. https://doi.org/10.1016/j.gr.2011.07.030

Ballèvre, M., Manzotti, P., & Dal Piaz, G. V. (2018). Pre-Alpine (Variscan) inheritance: A key for the location of the future Valaisan Basin (Western Alps). *Tectonics*, *37*, 786–817. https://doi.org/10.1002/2017TC004633

Bea, F., Montero, P., & Ortega, M. (2006). A LA-ICP-MS evaluation of Zr reservoirs in common crustal rocks: Implications for Zr and Hf geochemistry, and zircon-forming processes. *The Canadian Mineralogist*, *44*, 693–714. https://doi.org/10.2113/gscanmin.44.3.693

Bea, F., Morales, I., Molina, J. F., Montero, P., & Cambeses, A. (2021). Zircon stability grids in crustal partial melts: Implications for zircon inheritance. *Contributions to Mineralogy and Petrology*, *176*, 18. https://doi.org/10.1007/s00410-021-01772-x

Bearth, P. (1952). Geologie und petrographie des Monte Rosa. *Beiträge zur Geologischen Karte der Schweiz*, *96*, 1–94.

Bergomi, M. A., Dal Piaz, G. V., Malusà, M. G., Monopoli, B., & Tunesi, A. (2017). The grand St Bernard-Briançonnais nappe system and the Paleozoic inheritance of the Western Alps unraveled by zircon U-Pb dating. *Tectonics*, *36*, 2950–2972. https://doi.org/10.1002/2017TC004621

Biino, G. G., & Compagoni, R. (1992). Very-high pressure metamorphism of the Brossasco coronite metagranite, southern Dora-Maira Massif, Western Alps. *Schweizerische Mineralogische Und Petrographische Mitteilungen*, *72*, 347–363.

Borghi, A., Cadoppi, P., Porro, A., & Sacchi, R. (1985). Metamorphism in the northern part of the Dora-Maira Massif (Cottian Alps). *Bollettino del Museo Regionale di Scienze Naturali, Torino*, *3*, 369–380.

Borghi, A., Compagnoni, R., & Sandrone, R. (1996). Composite P-T paths in the internal Penninic massifs of the western Alps: Petrological constrains to their thermo-mechanical evolution. *Eclogae Geologicae Helvetiae*, *89*, 345–367.

Bouffette, J., Lardeaux, J. M., & Caron, J. M. (1993). Le passage des granulites aux éclogites dans les métapélites de l'unité de la Punta Muret (Massif Dora-Maira, Alpes occidentales). *Comptes Rendus de l'Académie des Sciences de Paris Serie II*, *317*, 1617–1624.

Bowhany, K., Hand, M., Clark, C., Kelsey, D. E., Reddy, S. M., Pearce, M. A., Tucker, N. M., & Morrissey, L. J. (2018). Phase equilibria modelling constraints on P-T conditions during fluid catalysed conversion of granulite to eclogite in the Bergen Arcs, Norway. *Journal of Metamorphic Geology*, *36*, 315–342. https://doi.org/10.1111/jmg.12294

Brandt, S., & Schenk, V. (2020). Metamorphic response to Alpine thrusting of a crustal-scale basement nappe in Southern Calabria (Italy). *Journal of Petrology*, *61*, egaa063. https://doi.org/10.1093/petrology/egaa063

Burri, M. (1983). Le front du Grand St-Bernard du val d'Hérens au val d'Aoste. *Eclogae Geologicae Helvetiae*, *76*, 469–490.

Bussy, F., & Cadoppi, P. (1996). U-Pb dating of granitoids from the Dora-Maira massif (western Italian Alps). *Schweizerische Mineralogische Und Petrographische Mitteilungen*, *76*, 217–233.

Bussy, F., Sartori, M., & Thélin, P. (1996). U-Pb zircon dating in the middle Penninic basement of the Western Alps (Valais, Switzerland). *Schweizerische Mineralogische Und Petrographische Mitteilungen*, *76*, 81–84.

Caddick, M. J., Konopásek, J., & Thompson, A. B. (2010). Preservation of garnet growth zoning and the duration of prograde metamorphism. *Journal of Petrology*, *51*, 2327–2347. https://doi.org/10.1093/petrology/egq059

Cadoppi, P. (1990). *Geologia del Basamento Cristallino nel Settore Settentrionale del Massiccio Dora-Maira (Alpi Occidentali)*. PhD's thesis. 208 pp.

Cadoppi, P., Camanni, G., Balestro, G., & Perrone, G. (2016). Geology of the Fontane talc mineralization (Germanasca valley, Italian Western Alps). *Journal of Maps*, *12*, 1170–1177. https://doi.org/10.1080/17445647.2016.1142480

Camacho, A., Compston, W., McCulloch, M., & McDougall, I. (1997). Timing and exhumation of eclogite facies shear zones, Musgrave Block, central Australia. *Journal of Metamorphic Geology*, *15*, 735–751. https://doi.org/10.1111/j.1525-1314.1997.00053.x

Castelli, D., Rolfo, F., Groppo, C., & Compagnoni, R. (2007). Impure marbles from the UHP Brossasco-Isasca Unit (Dora-Maira Massif, western Alps): Evidence for Alpine equilibration in the diamond stability field and evaluation of the X (CO_2) fluid evolution. *Journal of Metamorphic Geology*, *25*, 587–603. https://doi.org/10.1111/j.1525-1314.2007.00716.x

Cenki-Tok, B., Oliot, E., Rubatto, D., Berger, A., Engi, M., Janots, E., Thomsen, T. B., Manzottia, P., Regis, D., Spandler, C., Robyr, M., & Goncalves, P. (2011). Preservation of Permian allanite within an Alpine eclogite facies shear zone at Mt Mucrone, Italy: Mechanical and chemical behavior of allanite during mylonitization. *Lithos*, *125*, 40–50. https://doi.org/10.1016/j.lithos.2011.01.005

Chappell, B. W., & White, A. J. R. (2001). Two contrasting granite types: 25 years later. *Australian Journal of Earth Sciences*, *48*, 489–499. https://doi.org/10.1046/j.1440-0952.2001.00882.x

Chopin, C., Henry, C., & Michard, A. (1991). Geology and petrology of the coesite-bearing terrain, Dora-Maira massif, Western Alps. *European Journal of Mineralogy*, *3*, 263–291. https://doi.org/10.1127/ejm/3/2/0263

Cocco, F., Oggiano, G., Funedda, A., Loi, A., & Casini, L. (2018). Stratigraphic, magmatic and structural features of Ordovician tectonics in Sardinia (Italy): A review. *Journal of Iberian Geology*, *44*, 619–639. https://doi.org/10.1007/s41513-018-0075-1

Coggon, R., & Holland, T. J. B. (2002). Mixing properties of phengitic micas and revised garnet-phengite thermobarometers. *Journal of Metamorphic Geology*, *20*, 683–696. https://doi.org/10.1046/j.1525-1314.2002.00395.x

Compagnoni, R. (1977). The Sesia-Lanzo Zone: High pressure-low temperature metamorphism in the Austroalpine continental margin. *Rendiconti Della Societá Italiana di Mineralogia e Petrologia*, *33*, 335–374.

Compagnoni, R., Hirajima, T., & Chopin, C. (1995). Ultra-high-pressure metamorphic rocks in the Western Alps. In R. G. Coleman & X. Wang (Eds.), *Ultrahigh Pressure Metamorphism* (pp. 206–243). Cambridge University Press. https://doi.org/10.1017/CBO9780511573088.008

Compagnoni, R., & Maffeo, B. (1973). Jadeite-bearing metagranites l.s. and related rocks in the Mount Mucrone area (Sesia–Lanzo zone, Western Italian Alps). *Schweizerische Mineralogische und Petrographische Mitteilungen*, *53*, 355–378.

Compagnoni, R., & Rolfo, F. (2003). UHPM Units in the Western Alps. Ultrahigh-Pressure Units in the Western Alps. In D. A. Carswell & R. Compagnoni (Eds.), *Ultrahigh-pressure metamorphism*, European Mineralogical Union Notes in Mineralogy (Vol. 5, pp. 13–49). Eötvös University Press. https://doi.org/10.1180/EMU-notes.5.2

Compagnoni, R., Rolfo, F., Groppo, C., Hirajima, T., & Turello, R. (2012). Geological map of the ultra-high pressure Brossasco-Isasca unit (Western Alps, Italy). *Journal of Maps*, *8*, 465–472. https://doi.org/10.1080/17445647.2012.744367

Corfu, F., Hanchar, J. M., Hoskin, P. W. O., & Kinny, P. (2003). Atlas of zircon textures. *Reviews in Mineralogy and Geochemistry*, *53*, 469–500. https://doi.org/10.2113/0530469

Dal Piaz, G. V. (2001). Geology of the Monte Rosa massif: Historical review and personal comments. *Schweizerische Mineralogische Und Petrographische Mitteilungen*, *81*, 275–303.

De Capitani, C., & Brown, T. H. (1987). The computation of chemical equilibrium in complex systems containing non-ideal solutions. *Geochimica et Cosmochimica Acta*, *51*, 2639–2652. https://doi.org/10.1016/0016-7037(87)90145-1

De Capitani, C., & Petrakakis, K. (2010). The computation of equilibrium assemblage diagrams with Theriak/Domino software. *American Mineralogist*, *95*, 1006–1016. https://doi.org/10.2138/am.2010.3354

Détraz, G., & Loubat, H. (1984). Faciès à disthène, staurotide et grenat dans un micaschiste appartenant à l'unité des "gneiss du Sapey" (Vanoise, Alpes françaises). *Géologie Alpine*, *60*, 5–12.

Dickinson, W. R., & Gehrels, G. E. (2009). Use of U–Pb ages of detrital zircons to infer maximum depositional ages of strata: A test against a Colorado Plateau Mesozoic database. *Earth and Planetary Science Letters*, *288*, 115–125. https://doi.org/10.1016/j.epsl.2009.09.013

Diener, J. F. A., & Powell, R. (2012). Revised activity-composition models for clinopyroxene and amphibole. *Journal of Metamorphic Geology*, *30*, 131–142. https://doi.org/10.1111/j.1525-1314.2011.00959.x

Ellis, D. J., & Maboko, M. A. H. (1992). Precambrian tectonics and the physicochemical evolution of the continental crust. I. The gabbro-eclogite transition revisited. *Precambrian Research*, *55*, 491–506. https://doi.org/10.1016/0301-9268(92)90041-L

Engi, M., Scherrer, N. C., & Burri, T. (2001). Metamorphic evolution of pelitic rocks of the Monte Rosa nappe: Constraints from petrology and single grain monazite age data. *Schweizerische Mineralogische und Petrographische Mitteilungen*, *81*, 305–328.

Erambert, M., & Austrheim, H. (1993). The effect of fluid and deformation on zoning and inclusion patterns in poly-metamorphic garnets. *Contributions to Mineralogy and Petrology*, *115*, 204–214. https://doi.org/10.1007/BF00321220

Fedo, C. M., Sircombe, K. N., & Rainbird, R. H. (2003). Detrital zircon analysis of the sedimentary record. *Reviews in Mineralogy and Geochemistry*, *53*, 277–303. https://doi.org/10.2113/0530277

Feenstra, A., Petrakakis, K., & Rhede, D. (2007). Variscan relicts in Alpine high-P pelitic rocks from Samos (Greece): Evidence from multi-stage garnet and its included minerals. *Journal of Metamorphic Geology*, *25*, 1011–1033. https://doi.org/10.1111/j.1525-1314.2007.00741.x

Ferrando, S., Groppo, C., Frezzotti, M. L., Castelli, D., & Proyer, A. (2017). Dissolving dolomite in a stable UHP mineral assemblage: Evidence from Cal-Dol marbles of the Dora-Maira Massif (Italian Western Alps). *American Mineralogist*, *102*, 42–60. https://doi.org/10.2138/am-2017-5761

Franke, W., Ballèvre, M., Cocks, L. R. M., Torsvik, T. H., & Żelaźniewicz, A. (2020). Variscan orogeny. In *Encyclopedia of Geology* (2nd ed.). Elsevier. https://doi.org/10.1016/B978-0-08-102908-4.00022-9

Fréville, K., Trap, P., Faure, M., Melleton, J., Li, X-H., Lin, W., ... Poujol, M. (2018). Structural, metamorphic and geochronological insights on the Variscan evolution of the Alpine basement in the Belledonne Massif (France). *Tectonophysics*, *726*, 14–42. https://doi.org/10.1016/j.tecto.2018.01.017

Früh-Green, G. (1994). Interdependence of deformation, fluid infiltration and reaction progress recorded in eclogitic metagranitoids (Sesia Zone, Western Alps). *Journal of Metamorphic Geology*, *12*, 327–343. https://doi.org/10.1111/j.1525-1314.1994.tb00026.x

Gabudianu Radulescu, I., Compagnoni, R., & Lombardo, B. (2011). Polymetamorphic history of a relict Permian hornfels from the central Gran Paradiso Massif (Western Alps, Italy): A microstructural and thermodynamic modelling study. *Journal of Metamorphic Geology*, *29*, 851–874. https://doi.org/10.1111/j.1525-1314.2011.00943.x

Gaidies, F., Krenn, E., De Capitani, C., & Abart, R. (2008). Coupling forward modelling of garnet growth with monazite geochronology: An application to the Rappold Complex (Austroalpine crystalline basement). *Journal of Metamorphic Geology*, *26*, 775–793. https://doi.org/10.1111/j.1525-1314.2008.00787.x

Gaidies, F., Petley-Ragan, S., Chakraborty, S., Dasgupta, S., & Jones, P. (2015). Constraining the conditions of Barrovian metamorphism in Sikkim, India; P-T-t paths of garnet crystallization in the Lesser Himalayan Belt. *Journal of Metamorphic Geology*, *33*, 23–44. https://doi.org/10.1111/jmg.12108

Ganguly, J. (2010). Cation diffusion kinetics in aluminosilicate garnets and geological applications. *Reviews in Mineralogy and*

Geochemistry, *72*, 559–601. https://doi.org/10.2138/rmg.2010.72.12

Gasco, I., Gattiglio, M., & Borghi, A. (2011). Lithostratigraphic setting and P-T metamorphic evolution for the Dora-Maira Massif along the Piedmont Zone boundary (middle Susa Valley, NW Alps). *International Journal of Earth Sciences*, *100*, 1065–1085. https://doi.org/10.1007/s00531-011-0640-8

Gasquet, D., Bertrand, M., Paquette, J. L., Lehmann, J., Ratzov, G., de Guedes, R., & Nomade, S. (2010). Miocene to Messinian deformation and hydrothermal activity in a pre-Alpine basement massif of the French western Alps. *Bulletin de la Société Géologique de France*, *181*, 227–241. https://doi.org/10.2113/gssgfbull.181.3.227

Gauthiez-Putallaz, L., Rubatto, D., & Hermann, J. (2016). Dating prograde fluid pulses during subduction by in situ U–Pb and oxygen isotope analysis. *Contributions to Mineralogy and Petrology*, *171*, 15. https://doi.org/10.1007/s00410-015-1226-4

Gebauer, D., Schertl, H. P., Brix, M., & Schreyer, W. (1997). 35 Ma old ultrahigh-pressure metamorphism and evidence for very rapid exhumation in the Dora-Maira Massif, Western Alps. *Lithos*, *41*, 5–24. https://doi.org/10.1016/S0024-4937(97)82002-6

Giacomini, F., Braga, R., Tiepolo, M., & Tribuzio, R. (2007). New constraints on the origin and age of Variscan eclogitic rocks (Ligurian Alps, Italy). *Contributions to Mineralogy and Petrology*, *153*, 29–53. https://doi.org/10.1007/s00410-006-0131-2

Gilotti, J. A., McClelland, W. C., Coble, M. A., & Compagnoni, R. (2016). U-Pb SIMS analysis of jadeite-bearing orthogneiss at Tavagnasco Sesia Zone, Western Alps, Italy. *European Mineralogical Conference, Abstract*, 641.

Giorgis, D., Thelin, P., Stampfli, G., & Bussy, F. (1999). The Mont-Mort metapelites: Variscan metamorphism and geodynamic context (Brianqonnais basement, Western Alps, Switzerland). *Schweizerische Mineralogische Und Petrographische Mitteilungen*, *79*, 381–398.

Godard, G. (2009). Two orogenic cycles recorded in eclogite-facies gneiss from the southern Armorican Massif (France). *European Journal of Mineralogy*, *21*, 1173–1190. https://doi.org/10.1127/0935-1221/2009/0021-1984

Gosso, G., Rebay, G., Roda, M., Spalla, M. I., Tarallo, M., Zanoni, D., & Zucali, M. (2015). Taking advantage of petrostructural heterogeneities in subduction-collisional orogens, and effect on the scale of analysis. *Periodico di Mineralogia*, *84*, 779–825.

Gouffon, Y. (1993). Géologie de la "nappe" du Grand St-Bernard entre la Doire Baltée et la frontière suisse (Valle d'Aoste – Italie). *Mémoires de Géologie (Lausanne)*, *12*, 1–158.

Groppo, C., Beltrando, M., & Compagnoni, R. (2009). The P–T path of the ultra-high pressure Lago di Cignana and adjoining high-pressure meta-ophiolitic units: insights into the evolution of the subducting Tethyan slab. *Journal of Metamorphic Geology*, *27*, 207–231. https://doi.org/10.1111/j.1525-1314.2009.00814.x

Groppo, C., Castelli, D., & Compagnoni, R. (2006). Late chloritoid–staurolite assemblage in a garnet–kyanite-bearing metapelite from the ultrahigh-pressure Brossasco-Isasca unit (Dora-Maira Massif, Western Alps): New petrological constraints for a portion of the decompressional path. In Ultra-high pressure metamorphism: Deep continental subduction. *Geological Society of America Special Paper*, *403*, 127–138. https://doi.org/10.1130/2006.2403(07)

Groppo, C., Castelli, D., & Rolfo, F. (2007). HT, pre-Alpine relics in a spinel-bearing dolomite marble from the UHP Brossasco-Isasca Unit (Dora-Maira Massif, western Alps, Italy). *Periodico di Mineralogia*, *76*, 155–168.

Groppo, C., Ferrando, S., Gilio, M., Botta, S., Nosenzo, F., Balestro, G., Festa, A., & Rolfo, F. (2019). What's in the sandwich? New P–T constraints for the (U)HP nappe stack of southern Dora-Maira Massif (Western Alps). *European Journal of Mineralogy*, *31*, 665–683.

Groppo, C., Rolfo, F., & Lombardo, B. (2009). P–T evolution across the Main Central Thrust Zone (Eastern Nepal): Hidden discontinuities revealed by petrology. *Journal of Petrology*, *50*, 1149–1180. https://doi.org/10.1093/petrology/egp036

Jacob, J.-B., Guillot, S., Rubatto, D., Janots, E., Melleton, J., & Faure, M. (2021). Carboniferous high pressure metamorphism and deformation in the Belledonne Massif (Western Alps). *Journal of Metamorphic Geology*, *39*, 1009–1044. https://doi.org/10.1111/jmg.12600

Hacker, B., Kylander-Clark, A., & Holder, R. (2019). REE partitioning between monazite and garnet: Implications for petrochronology. *Journal of Metamorphic Geology*, *37*, 227–237. https://doi.org/10.1111/jmg.12458

Handy, M. R., Schmid, S. M., Bousquet, R., Kissling, E., & Bernoulli, D. (2010). Reconciling plate-tectonic reconstructions of Alpine Tethys with the geological–geophysical record of spreading and subduction in the Alps. *Earth-Science Reviews*, *102*, 121–158. https://doi.org/10.1016/j.earscirev.2010.06.002

Hawemann, F., Mancktelow, N. S., Wex, S., Camacho, A., & Pennacchioni, G. (2018). Pseudotachylite as field evidence for lower-crustal earthquakes during the intracontinental Petermann Orogeny (Musgrave Block, central Australia). *Solid Earth*, *9*, 629–648. https://doi.org/10.5194/se-9-629-2018

Heinrichs, T., Siegesmund, S., Frei, D., Drobe, M., & Schulz, B. (2012). Provenance signatures from whole-rock geochemistry and detrital zircon ages of metasediments from the Austroalpine basement south of the Tauren window (eastern Tyrol, Austria). *Geo. Alp*, *9*, 156–185.

Henry, C. (1990). *L'unité à coesite du massif Dora-Maira dans son cadre pétrologique et structural (Alpes Occidentales, Italie)*. PhD's thesis, Université, 149 pp.

Henry, C., Michard, A., & Chopin, C. (1993). Geometry and structural evolution of ultra-high pressure and high pressure rocks from the Dora-Maira massif, western Alps, Italy. *Journal of Structural Geology*, *15*, 965–981. https://doi.org/10.1016/0191-8141(93)90170-F

Hoiland, C. W., Miller, E. L., & Pease, V. (2018). Greenschist facies metamorphic zircon overgrowths as a constraint on exhumation of the Brooks Range metamorphic core. *Alaska. Tectonics*, *37*, 3429–3455. https://doi.org/10.1029/2018TC005006

Holland, T. J. B., & Powell, R. (1998). An internally consistent thermodynamic data set for phases of petrological interest. *Journal of Metamorphic Geology*, *16*, 309–343. https://doi.org/10.1111/j.1525-1314.1998.00140.x

Holland, T. J. B., & Powell, R. (2003). Activity-composition relations for phases in petrological calculations: An asymmetric multicomponent formulation. *Contributions to Mineralogy and Petrology*, *145*, 492–501. https://doi.org/10.1007/s00410-003-0464-z

Horstwood, M. S. A., Košler, J., Gehrels, G., Jackson, S. E., Mc, L. N., Paton, C., Pearson, N. J., Sircombe, K., Sylvester, P., Vermeesch, P., Bowring, J. F., Condon, D. J., & Schoene, B.

(2016). Community-derived standards for LA-ICP-MS U-(Th-) Pb geochronology—Uncertainty propagation, age interpretation and data reporting. *Geostandards and Geoanalytical Research*, *40*, 311–332. https://doi.org/10.1111/j.1751-908X.2016.00379.x

Hoskin, P. W. O., & Schaltegger, U. (2003). The composition of zircon and igneous and metamorphic petrogenesis. *Reviews in Mineralogy and Geochemistry*, *53*, 27–62. https://doi.org/10.2113/0530027

Jackson, S. E., Pearson, N. J., Griffin, W. L., & Belousova, E. A. (2004). The application of laser ablation-inductively coupled plasma-mass spectrometry to in situ U–Pb zircon geochronology. *Chemical Geology*, *211*, 47–69. https://doi.org/10.1016/j.chemgeo.2004.06.017

Jamtveit, B., Bucher-Nurminen, K., & Austrheim, H. (1991). Fluid controlled eclogitization of granulites in deep crustal shear zones, Bergen arcs, Western Norway. *Contributions to Mineralogy and Petrology*, *104*, 184–193.

Kelsey, D. E., Clark, C., & Hand, M. (2008). Thermobarometric modelling of zircon and monazite growth in melt-bearing systems: Examples using model metapelitic and metapsammitic granulites. *Journal of Metamorphic Geology*, *26*, 199–212. https://doi.org/10.1111/j.1525-1314.2007.00757.x

Kelsey, D. E., & Powell, R. (2011). Progress in linking accessory mineral growth and breakdown to major mineral evolution in metamorphic rocks: A thermodynamic approach in the Na_2O-CaO-K_2O-FeO-MgO-Al_2O_3-SiO_2-H_2O-TiO_2-ZrO_2 system. *Journal of Metamorphic Geology*, *29*, 151–166. https://doi.org/10.1111/j.1525-1314.2010.00910.x

Kohn, M. J., Corrie, S. L., & Markley, C. (2015). The fall and rise of metamorphic zircon. *American Mineralogist*, *100*, 897–908. https://doi.org/10.2138/am-2015-5064

Koons, P. O., Rubie, D., & Früh-Green, G. (1987). The effect of disequilibrium and deformation on the mineralogical evolution of quartz diorite during metamorphism in the eclogite facies. *Journal of Petrology*, *28*, 679–700. https://doi.org/10.1093/petrology/28.4.679

Krabbendam, M., Wain, A., & Andersen, T. B. (2000). Precaledonian granulite and gabbro enclaves in the Western Gneiss Region, Norway: Indications of incomplete transition at high pressure. *Geological Magazine*, *137*, 235–255. https://doi.org/10.1017/S0016756800004015

Kunz, B. E., Manzotti, P., von Niederhäusern, B., Engi, M., Darling, J. R., Giuntoli, F., … Lanari, P. (2018). Permian high-temperature metamorphism in the Western Alps (NW Italy). *International Journal of Earth Sciences*, *107*, 203–229. https://doi.org/10.1007/s00531-017-1485-6

Lardeaux, J. M., Schwartz, S., Tricart, P., Paul, A., Guillot, S., Béthoux, N., … Masson, F. (2006). A crustal-scale cross-section of the south-western Alps combining geophysical and geological imagery. *Terra Nova*, *18*, 412–422. https://doi.org/10.1111/j.1365-3121.2006.00706.x

Le Bayon, B., Pitra, P., Ballèvre, M., & Bohn, M. (2006). Reconstructing P–T paths during continental collision using multi-stage garnet (Gran Paradiso nappe, Western Alps). *Journal of Metamorphic Geology*, *24*, 477–496. https://doi.org/10.1111/j.1525-1314.2006.00649.x

Lenze, A., & Stöckhert, B. (2007). Microfabrics of UHP metamorphic granites in the Dora-Maira Massif, western Alps—No evidence for deformation at great depths. *Journal of Metamorphic Geology*, *25*, 461–475. https://doi.org/10.1111/j.1525-1314.2007.00707.x

Liati, A., Gebauer, D., & Fanning, M. (2009). Geochronological evolution of HP metamorphic rocks of the Adula nappe, Central Alps, in pre-Alpine and Alpine subduction cycles. *Journal of the Geological Society, London*, *166*, 797–810. https://doi.org/10.1144/0016-76492008-033

Liermann, H. P., Isachsen, C., Altenberger, U., & Oberhänsli, R. (2002). Behavior of zircon during high-pressure, lowtemperature metamorphism: Case study from the internal unit of the Sesia zone (Western Italian Alps). *European Journal of Mineralogy*, *14*, 61–71. https://doi.org/10.1127/0935-1221/2002/0014-0061

Lopez-Sanchez, M. A., Aleinikoff, J. N., Marcos, A., Martínez, F. J., & Llana-Fúnez, S. (2016). An example of low-Th/U zircon overgrowths of magmatic origin in a late orogenic Variscan intrusion: The San Ciprián massif (NW Spain). *Journal of the Geological Society*, *173*, 282–291. https://doi.org/10.1144/jgs2015-071

Lund, M. G., & Austrheim, H. (2003). High-pressure metamorphism and deep-crustal seismicity: Evidence from contemporaneous formation of pseudotachylites and eclogite-facies coronas. *Tectonophysics*, *372*, 59–83. https://doi.org/10.1016/S0040-1951(03)00232-4

Mahar, E. M., Baker, J., Powell, R., Holland, T. J. B., & Howell, N. (1997). The effect of Mn on mineral stability in metapelites. *Journal of Metamorphic Geology*, *15*, 223–238. https://doi.org/10.1111/j.1525-1314.1997.00011.x

Malusà, M. G., Carter, A., Limoncelli, M., Villa, I. M., & Garnzanti, E. (2013). Bias in detrital zircon geochronology and thermochronometry. *Chemical Geology*, *359*, 90–107. https://doi.org/10.1016/j.chemgeo.2013.09.016

Mandl, M., Kurz, W., Hauzenberger, C., Fritz, H., Klötzli, U., & Schuster, R. (2018). Pre-Alpine evolution of the Seckau Complex (Austroalpine basement/Eastern Alps): Constraints from in-situ LA-ICP-MS U-Pb zircon geochronology. *Lithos*, *296*, 412–430. https://doi.org/10.1016/j.lithos.2017.11.022

Manzotti, P., & Ballèvre, M. (2013). Multistage garnet in high-pressure metasediments: Alpine overgowths on Variscan detrital grains. *Geology*, *41*, 1151–1154. https://doi.org/10.1130/G34741.1

Manzotti, P., Ballèvre, M., Pitra, P., & Schiavi, F. (2021). Missing lawsonite and aragonite found: P-T and fluid composition in meta-marls from the Combin Zone (Western Alps). *Contributions to Mineralogy and Petrology*, *176*, 60. https://doi.org/10.1007/s00410-021-01818-0

Manzotti, P., Ballèvre, M., & Poujol, M. (2016). Detrital zircon geochronology in the Dora-Maira and Zone Houillère: A record of sediment travel paths in the Carboniferous. *Terra Nova*, *28*, 279–288. https://doi.org/10.1111/ter.12219

Manzotti, P., Bosse, V., Pitra, P., Robyr, M., Schiavi, F., & Ballèvre, M. (2018). Exhumation rates in the Gran Paradiso Massif (Western Alps) constrained by in situ U–Th–Pb dating of accessory phases (monazite, allanite and xenotime). *Contributions to Mineralogy and Petrology*, *173*, 24. https://doi.org/10.1007/s00410-018-1452-7

Manzotti, P., Pitra, P., Langlade, J., & Ballèvre, M. (2015). Constraining P–T conditions during thrusting of a higher pressure

unit over a lower pressure one (Gran Paradiso, Western Alps). *Journal of Metamorphic Geology*, *33*(9), 981–1002. https://doi.org/10.1111/jmg.12156

Manzotti, P., Poujol, M., & Ballèvre, M. (2015). Detrital zircon geochronology in blueschist-facies meta-conglomerates from the Western Alps: Implications for the late Carboniferous to early Permian palaeogeography. *International Journal of Earth Sciences*, *104*, 703–731. https://doi.org/10.1007/s00531-014-1104-8

Manzotti, P., Rubatto, D., Zucali, M., El Korh, A., Cenki-Tok, B., Ballèvre, M., & Engi, M. (2018). Permian magmatism and metamorphism in the Dent Blanche nappe: Constraints from field observations and geochronology. *Swiss Journal of Geosciences*, *111*, 79–97. https://doi.org/10.1007/s00015-017-0284-1

Matsumoto, N., & Hirajima, T. (2000). Gamet in pelitic schists from a quartz-eclogite unit of the southern Dora-Maira massif, Western Alps. *Schweizerische Mineralogische Und Petrographische Mitteilungen*, *80*, 53–62.

McDonough, W. F., & Sun, S. S. (1995). The composition of the Earth. *Chemical Geology*, *120*, 223–253. https://doi.org/10.1016/0009-2541(94)00140-4

Messiga, B., Tribuzio, R., & Caucia, F. (1992). Amphibole evolution in Variscan eclogite-amphibolites from the Savona crystalline massif (western Ligurian Alps, Italy): Controls on the decompressional P–T–t path. *Lithos*, *27*, 215–230. https://doi.org/10.1016/0024-4937(91)90001-2

Michard, A. (1967). *Etudes Géologiques dans les Zones Internes des Alpes Cottiennes*. CNRS éditions. 447 pp. (available online at https://tel.archives-ouvertes.fr/tel-00802836).

Michard, A., Chopin, C., & Henry, C. (1993). Compression versus extension in the exhumation of the Dora-Maira coesite-bearing unit, Western Alps, Italy. *Tectonophysics*, *221*, 173–193. https://doi.org/10.1016/0040-1951(93)90331-D

Miller, C. F., McDowell, S. M., & Mapes, R. W. (2003). Hot and cold granites? Implications of zircon saturation temperatures and preservation of inheritance. *Geology*, *31*, 529–532. DOI: 10.1130/0091-7613(2003)031<0529:HACGIO>2.0.CO;2

Novarese, V. (1895). Sul rilevamento eseguito nel 1894 in valle della Germanasca (Alpi Cozie). *Bollettino del Reale Comitato Geologico d'Italia*, *26*, 253–282.

Novarese, V. (1898). I giacimenti di grafite delle Alpi Cozie. *Bollettino del Reale Comitato Geologico d'Italia*, *29*, 3–35.

Novarese, V. (1905). La grafite nelle Alpi piemontesi. *Atti Della Accademia Reale Delle Scienze di Torino*, *40*, 1–16.

Paoli, G., Stokke, H. H., Rocchi, S., Sirevaag, H., Ksienzyk, A. K., Jacobs, J., & Košler, J. (2017). Basement provenance revealed by U–Pb detrital zircon ages: A tale of African and European heritage in Tuscany, Italy. *Lithos*, *277*, 376–387. https://doi.org/10.1016/j.lithos.2016.11.017

Paquette, J. L., & Tiepolo, M. (2007). High resolution (5 μm) U–Th–Pb isotope dating of monazite with excimer laser ablation (ELA)-ICPMS. *Chemical Geology*, *240*(3–4), 222–237. https://doi.org/10.1016/j.chemgeo.2007.02.014

Paton, C., Hellstrom, J., Paul, B., Woodhead, J., & Hergt, J. (2011). Iolite: Freeware for the visualisation and processing of mass spectrometric data. *Journal of Analytical Atomic Spectrometry*, *26*, 2508–2518. https://doi.org/10.1039/c1ja10172b

Paton, C., Woodhead, J. D., Hellstrom, J. C., Herget, J. M., Greig, A., & Maas, R. (2010). Improved laser ablation U-Pb zircon geochronology through robust downhole fractionation correction. *Geochemistry, Geophysics, Geosystems*, *11*(3), Q0AA06. https://doi.org/10.1029/2009GC002618

Petri, B., Mohn, G., Štípská, P., Schulmann, K., & Manatschal, G. (2016). The Sondalo gabbro contact aureole (Campo unit, Eastern Alps): Implications for mid-crustal mafic magma emplacement. *Contributions to Mineralogy and Petrology*, *171*, 52. https://doi.org/10.1007/s00410-016-1263-7

Pieruccioni, D., Vezzoni, S., & Petrelli, M. (2018). A petrographic and U-Pb geochronological approach to the reconstruction of the pre-Alpine history of Alpi Apuane (Tuscany). *Atti Della Società Toscana di Scienze Naturali – Memorie Serie A*, *125*, 69–80.

Pillola, G. L., Leone, F., & Loi, A. (1998). The Cambrian and early Ordovician of SW Sardinia. *Giornale di Geologia*, *60*, 25–38.

Pondrelli, M., Corradini, C., Spalletta, C., Simonetto, L., Perri, M. C., Corriga, M. G., Venturini, C., & Schönlaub, H. P. (2020). Geological map and stratigraphic evolution of the central sector of the Carnic Alps (Austria-Italy). *Italian Journal of Geosciences*, *139*, 469–484. https://doi.org/10.3301/IJG.2020.16

Pouclet, A., Alvaro, J. J., Bardintzeff, J.-M., Gil Ilmaz, A., Monceret, E., & Vizcaïno, D. (2017). Cambrian-early Ordovician volcanism across the South Armorican and Occitan domains of the Variscan belt in France: Continental break-up and rifting of the northern Gondwana margin. *Geoscience Frontiers*, *8*, 25–64. https://doi.org/10.1016/j.gsf.2016.03.002

Pownceby, M. I., Wall, V. J., & O' Neil, H. C. (1991). An experimental study of the effect of Ca upon garnet-llmenite Fe-Mn exchange equilibria. *American Mineralogist*, *76*, 1580–1588.

Rahn, M. (1991). Eclogites from the Minugrat, Siviez-Mischabel nappe (Valais, Switzerland). *Schweizerische Mineralogische Und Petrographische Mitteilungen*, *71*, 415–426.

Ramsay, J. G., & Allison, I. (1979). Structural analysis of shear zones in an alpinised Hercynian granite (Maggia Lappen, Pennine zone, Central Alps). *Schweizerische Mineralogische Und Petrographische Mitteilungen*, *59*, 251–279.

Regis, D., Warren, C. J., Young, D., & Roberts, N. M. W. (2014). Tectono-metamorphic evolution of the Jomolhari massif: Variations in timing of syn-collisional metamorphism across western Bhutan. *Lithos*, *190*, 449–466. https://doi.org/10.1016/j.lithos.2014.01.001

Robyr, M., Darbellay, B., & Baumgartner, L. P. (2014). Matrix-dependent garnet-growth in polymetamorphic rocks of the Sesia Zone, Italian Alps. *Journal of Metamorphic Geology*, *32*, 3–24. https://doi.org/10.1111/jmg.12055

Rubatto, D. (2002). Zircon trace element geochemistry: partitioning with garnet and the link between U–Pb ages and metamorphism. *Chemical Geology*, *184*, 123–138. https://doi.org/10.1016/S0009-2541(01)00355-2

Rubatto, D. (2017). Zircon: The metamorphic mineral. *Reviews in Mineralogy & Geochemistry*, *83*, 261–295. https://doi.org/10.2138/rmg.2017.83.9

Rubatto, D., Ferrando, S., Compagnoni, R., & Lombardo, B. (2010). Carboniferous high-pressure metamorphism of Ordovician protoliths in the Argentera Massif (Italy), Southern European Variscan belt. *Lithos*, *116*, 65–76. https://doi.org/10.1016/j.lithos.2009.12.013

Rubatto, D., & Hermann, J. (2001). Exhumation as fast as subduction? *Geology*, *29*, 3–6. 10.1130/0091-7613(2001)029<0003:EAFAS>2.0.CO;2

Sandmann, S., Nagel, T. J., Herwartz, D., Fonseca, R. O. C., Kurzawski, R. M., Münker, C., … Froitzhein, N. (2014). Lu–Hf garnet systematics of a polymetamorphic basement unit: New evidence for coherent exhumation of the Adula Nappe (Central Alps) from eclogite-facies conditions. *Contributions to Mineralogy and Petrology*, *168*, 1075. https://doi.org/10.1007/s00410-014-1075-6

Sandrone, R., & Borghi, A. (1992). Zoned garnets in the northern Dora-Maira Massif and their contribution to a reconstruction of the regional metamorphic evolution. *European Journal of Mineralogy*, *4*, 465–474. https://doi.org/10.1127/ejm/4/3/0465

Sandrone, R., Cadoppi, P., Sacchi, R., & Vialon, P. (1993). The Dora-Maira massif. In *Pre-Mesozoic geology in the Alps* (pp. 317–325). Springer. https://doi.org/10.1007/978-3-642-84640-3_18

Sartori, M. (1990). L'unité du Barrhorn (Zone pennique, Valais, Suisse). In *Mémoires de Géologie Lausanne* (Vol. 5, p. 156). Lausanne: Mémoires de Géologie Lausanne.

Schmid, S. M., Fügenschuh, B., Kissling, E., & Schuster, R. (2004). Tectonic map and overall architecture of the Alpine orogeny. *Eclogae Geologicae Helvetiae*, *97*, 93–117. https://doi.org/10.1007/s00015-004-1113-x

Schuster, R., & Stüwe, K. (2008). Permian metamorphic event in the Alps. *Geology*, *36*, 603–606. https://doi.org/10.1130/G24703A.1

Sireevag, H., Jacobs, J., Ksienzyk, A. K., Rocchi, S., Paoli, G., Jørgensen, H., & Košler, J. (2016). From Gondwana to Europe: The journey of Elba Island (Italy) as recorded by U–Pb detrital zircon ages of Paleozoic metasedimentary rocks. *Gondwana Research*, *38*, 273–288.

Sláma, J., & Košler, J. (2012). Effects of sampling and mineral separation on accuracy of detrital zircon studies. *Geochemistry, Geophysics, Geosystems*, *13*(5), Q05007. https://doi.org/10.1029/2012GC004106

Sláma, J., Košler, J., Condon, D. J., Crowley, J. L., Gerdes, A., Hanchar, J. M., … Whitehouse, J. M. (2008). Plesovice zircon—A new natural reference material for U-Pb and Hf isotopic microanalysis. *Chemical Geology*, *249*, 1–35. https://doi.org/10.1016/j.chemgeo.2007.11.005

Spiess, R., Groppo, C., & Compagnoni, R. (2007). When epitaxy controls garnet growth. *Journal of Metamorphic Geology*, *25*, 439–450. https://doi.org/10.1111/j.1525-1314.2007.00704.x

Thélin, P. (1992). Les métapélites du Mont-Mort: une fenêtre métamorphique (Nappe des Pontis, Zone du Ruitor, Valais). *Bulletin de la Société Vaudoise Des Sciences Naturelles*, *82*, 97–116.

Thélin, P., Sartori, M., Lengeler, R., & Schaerer, J.-P. (1990). Eclogites of Paleozoic or early Alpine age in the basement of the Penninic Siviez-Mischabel nappe, Wallis, Switzerland. *Lithos*, *25*, 71–88. https://doi.org/10.1016/0024-4937(90)90007-N

Vaughan-Hammon, J. D., Luisier, C., Baumgartner, L. P., & Schmalholz, S. M. (2021). Peak Alpine metamorphic conditions from staurolite-bearing metapelites in the Monte Rosa nappe (central European Alps) and geodynamic implications. *Journal of Metamorphic Geology*, *39*, 897–917. https://doi.org/10.1111/jmg.12595

Vermeesch, P. (2004). How many grains are needed for a provenance study? *Earth and Planetary Science Letters*, *224*, 441–451. https://doi.org/10.1016/j.epsl.2004.05.037

Vermeesch, P. (2018). IsoplotR: A free and open toolbox for geochronology. *Geoscience Frontiers*, *9*, 1479–1493. https://doi.org/10.1016/j.gsf.2018.04.001

Vialon, P. (1966). Étude géologique du massif cristalline Dora-Maira, Alpes Cottiennes Internes, Italie. Travaux du Laboratoire de Géologie de la Faculté des Sciences de Grenoble, Mémoires, 4, 293 pp. (accessible online at https://hal.archives-ouvertes.fr/tel-00723197).

Wei, C. J., & Powell, R. (2004). Calculated phase relations in high-pressure metapelites in the system NKFMASH (Na_2O-K_2O-FeO-MgO-Al_2O_3-SiO_2-H_2O). *Journal of Petrology*, *45*, 183–202. https://doi.org/10.1093/petrology/egg085

White, R. W., Pomroy, N. E., & Powell, R. (2005). An in-situ metatexite-diatexite transition in upper amphibolite facies rocks from Broken Hill, Australia. *Journal of Metamorphic Geology*, *23*, 579–602. https://doi.org/10.1111/j.1525-1314.2005.00597.x

White, R. W., Powell, R., & Holland, T. J. B. (2007). Progress relating to calculation of partial melting equilibria for metapelites. *Journal of Metamorphic Geology*, *25*, 511–527. https://doi.org/10.1111/j.1525-1314.2007.00711.x

White, R. W., Powell, R., Holland, T. J. B., & Worley, B. (2000). The effect of TiO2 and Fe2O3 on metapelitic assemblages at greenschist and amphibolite facies conditions: Mineral equilibria calculations in the system K_2O-FeO-MgO-Al_2O_3-SiO_2-H_2O-TiO_2-Fe_2O_3. *Journal of Metamorphic Geology*, *18*, 497–511. https://doi.org/10.1046/j.1525-1314.2000.00269.x

Woodhead, J. D., Hellstrom, J., Hergt, J. M., Greig, A., & Maas, R. (2007). Isotopic and elemental imaging of geological materials by laser ablation inductively coupled plasma-mass spectrometry. *Geostandards and Geoanalytical Research*, *31*, 331–342. https://doi.org/10.1111/j.1751-908X.2007.00104.x

Xiong, J.-W., Chen, Y.-X., Zhou, K., Schertl, H.-P., Zheng, Y.-F., Huang, F., … Chen, Z.-W. (2021). Fe and O isotopes in coesite-bearing jadeite quartzite from the Western Alps record multi-stage fluid-rock interactions in a continental subduction zone. *Geochimica et Cosmochimica Acta*, *312*, 1–24. https://doi.org/10.1016/j.gca.2021.08.006

Yardley, B. W. D. (1977). An empirical study of diffusion in garnet. *American Mineralogist*, *62*, 793–800.

Zhang, R. Y., & Liou, J. G. (1997). Partial transformation of gabbro to coesite bearing eclogite from Yangkou, the Sulu terrain, eastern China. *Journal of Metamorphic Geology*, *15*, 183–202. https://doi.org/10.1111/j.1525-1314.1997.00012.x

SUPPORTING INFORMATION

Additional supporting information may be found in the online version of the article at the publisher's website.

Appendix S1. Operating conditions for microprobe analyses.

Appendix S2. Mineral abbreviations.

Appendix S3. Symbols

Appendix S4. Operating conditions of LA-ICP-MS equipment for U-Pb zircon dating.

Appendix S5. Operating conditions of LA-ICP-MS equipment for U-Th-Pb monazite dating.

Appendix S6. Garnet fractionation method.

Figure S1. Analysed garnet porphyroblast and its inclusions.
Figure S2. Pre-Alpine muscovite overgrown by Alpine muscovite.
Figure S3. Monazite U-Th-Pb dating and REE partitioning with garnet.
Figure S4. AFM chemical diagram.
Figure S5. Calculated modal amounts of biotite.
Figure S6. Calculated mineral modal amount.

Table S1. Representative chemical analyses of main minerals in OG27.
Table S2. Representative chemical analyses of main minerals in GM1.
Table S3. Representative chemical analyses of main minerals in GM13.
Table S4. Bulk-rock compositions.
Table S5. Results of garnet-ilmenite thermometry.
Table S6. Results of U-Pb zircon analyses in OG27.
Table S7. Results of U-Pb zircon analyses in GM1.
Table S8. Results of U-Pb zircon analyses in GM13.
Table S9. Results of U-Th-Pb monazite dating in GM1.
Table S10. Zircon trace element composition in OG27.
Table S11. Garnet trace element composition in GM1.
Table S12. Zircon trace element composition in GM1.
Table S13. Monazite trace element composition in GM1.

How to cite this article: Nosenzo, F., Manzotti, P., Poujol, M., Ballèvre, M., & Langlade, J. (2022). A window into an older orogenic cycle: *P–T* conditions and timing of the pre-Alpine history of the Dora-Maira Massif (Western Alps). *Journal of Metamorphic Geology*, 1–33. https://doi.org/10.1111/jmg.12646